Engaging Biological Oscillators through Second Messenger Pathways Permits Emergence of a Robust Gastric Slow-Wave during Peristalsis

Short Title: Emergence of Robust Gastric Slow-Wave during Peristalsis

Md Ashfaq Ahmed[1], Sharmila Venugopal[2*], Ranu Jung[1*]

[1]Department of Biomedical Engineering, Florida International University, Miami, Florida, United States of America.

[2]Integrative Biology and Physiology, University of California Los Angeles, Los Angeles, California, United States of America.

* Corresponding authors

E-mail: RJung@fiu.edu; vsharmila@ucla.edu

Conflict of Interest Statement:

The authors declare no conflict of interest.

1

20 **Data Availability Statement:**

24 **Keywords:**

Abstract

27 Peristalsis, the coordinated contraction - relaxation of the muscles of the stomach is important for

28 normal gastric motility and is impaired in motility disorders. Coordinated electrical depolarizations

29 that originate and propagate within a network of interconnected layers of interstitial cells of Cajal

30 (ICC) and smooth muscle (SM) cells of the stomach wall as a slow-wave, underly peristalsis.

31 Normally, the gastric slow-wave oscillates with a single period and uniform rostrocaudal lag,

32 exhibiting network entrainment. Understanding of the integrative role of neurotransmission and

33 intercellular coupling in the propagation of an entrained gastric slow-wave, important for

34 understanding motility disorders, however, remains incomplete. Using a computational framework

35 constituted of a novel gastric motility network (GMN) model we address the hypothesis that

36 engaging biological oscillators (i.e., ICCs) by constitutive gap junction coupling mechanisms and

37 enteric neural stimulus activated signals can confer a robust entrained gastric slow-wave. We

38 demonstrate that while a decreasing enteric neural stimulus gradient that modulates the

39 intracellular IP_3 concentration in the ICCs can guide the aboral slow-wave propagation essential

40 for peristalsis, engaging ICCs by recruiting the exchange of second messengers (inositol

41 trisphosphate (IP_3) and Ca^{2+}) ensures a robust entrained longitudinal slow-wave, even in the

42 presence of biological variability in coupling strengths. Our GMN with the distinct intercellular

2

43   coupling in conjunction with the intracellular feedback pathways and a rostrocaudal enteric neural

44   stimulus gradient allows gastric slow waves to oscillate with a moderate range of frequencies and

45   to propagate with a broad range of velocities, thus preventing decoupling observed in motility

46   disorders. Overall, the findings provide a mechanistic explanation for the emergence of decoupled

47   slow waves associated with motility impairments of the stomach, offer directions for future

48   experiments and theoretical work, and can potentially aid in the design of new interventional

49   pharmacological and neuromodulation device treatments for addressing gastric motility disorders.

Author Summary

51   The coordinated contraction and relaxation of the muscles of the stomach, known as peristalsis

52   is important for normal gastric motility and primarily governed by electrical depolarizations that

53   originate and propagate within a network of interconnected layers of interstitial cells of Cajal

54   (ICCs) and smooth muscle cells of the stomach wall as a slow-wave. Under normal conditions, a

55   gastric slow-wave oscillates with a single period and uniform rostrocaudal lag, exhibiting network

56   entrainment. However, the understanding of intrinsic and extrinsic mechanisms that ensure

57   propagation of a robust entrained slow-wave remains incomplete. Here, using a computational

58   framework, we show that in conjunction with an enteric neural stimulus gradient along the

59   rostrocaudal ICC chain, and intercellular electrical coupling, the intercellular exchange of inositol

60   trisphosphate between ICCs prevents decoupling by extending the longitudinal entrainment range

61   along the stomach wall, even when variability in intercellular coupling exists. The findings from

62   our study indicate ways that ensure the rostrocaudal spread of a robust gastric slow-wave and

63   provide a mechanistic explanation for the emergence of decoupled slow waves associated with

64   motility impairments of the stomach.

65

66

67

Introduction

Gastric peristalsis, the coordinated contraction and relaxation of the muscles of the stomach, is a critical phenomenon for food propulsion and waste product elimination [1] and is impaired in motility disorders [2–4]. The coordination of the contractions along the rostrocaudal compartments of the stomach causes rhythmic longitudinally travelling aboral muscle contractions [5]. Sometimes in motility disorders, the contractions can occur at a faster rate than the usual (tachygastria) or at a slower rate (bradygastria) [4,6]; whereas in some cases the rostrocaudal coordination of contractions is lost resulting in decoupling (the activity of the caudal end and the rostral end become independent of each other) or functional uncoupling (the activity of the caudal end controlling the activity of the rostral end [7,8]) of contractions in the stomach [9]. Events like these have been associated with gastric motility disorders such as gastroparesis (delay in food transit), functional dyspepsia and gastroesophageal reflux disease [4,6,10].

Peristalsis is governed by diverse and overlapping mechanisms which normally ensure robust motility patterns. Peristalsis emerges from a mutually coupled chain of pacemaker cells called the interstitial cells of Cajal (ICCs). The ICCs can independently generate electrical activity known as pacemaker potentials, which drive rhythmic potentials in the circular and longitudinal smooth muscle (SM) cells embedded in the stomach wall [5,11–13]. The electrical activity propagates through this network of cells in a coordinated manner resulting in gastric slow-wave (GSW) propagation [13,14] that underlies peristalsis.

The propagation is enabled in part by gap junction channels between the ICCs, between ICCs and SM cells, as well as between SM cells [15–17]. The SM cells, lacking intrinsic pacemaker capability, do not regenerate the slow-wave. Regeneration of the gastric slow-wave instead occurs within the pacemaker ICCs. Without coordinated ICC-ICC interactions, gastric slow-wave events do not propagate long distances [18]. Therefore, understanding how coordination arises

4

92   between ICCs for propagating the gastric slow-wave is critical for understanding abnormal

93   peristalsis that is present in gastric motility disorders.

94   A causal relationship between electrical gap-junction coupling in a network of ICCs and the

95   emergent gastric slow-wave has been unequivocally demonstrated by computational studies

96   (e.g., [7,8,19]). Pacemaker ICCs contain calcium (Ca^{2+}) and inositol 1,4,5- trisphosphate (IP_3)

97   within their cytoplasm [20,21]. Gap junctions also facilitate exchange of second messengers such

98   as Ca^{2+} and IP_3 between adjacent cells [22–25]. Such exchange of Ca^{2+} and IP_3 can impact

99   intracellular concentration of Ca^{2+} and IP_3 within pacemaker cells and therefore, can modulate the

100   oscillation frequency of the concerned cell. In addition, the intracellular concentration of IP_3 is

101   modulated by the enteric neural stimuli received by the ICC [26–29]. Therefore, understanding

102   the role of second messengers and their neural control is likely important for understanding

103   aberrations in slow-wave propagation that result in the emergence of gastric motility disorders.

104   The longitudinally arranged ICCs along the stomach wall with intercellular gap junctions, resemble

105   a chain of coupled oscillators [30,31]. In such a chain, the rostral or leading oscillator can gradually

106   engage the trailing oscillators along the chain such that, at a steady-state, all the oscillators are

107   frequency and phase-locked, with a constant phase lag between consecutive oscillators [32–34].

108   This phenomenon known as oscillator entrainment is thought to be the basis for the GSW in the

109   stomach [30,31]. The integrative role of neurotransmission and intercellular coupling mechanisms

110   in GSW entrainment remain incompletely understood. To distinguish the intercellular exchange

111   of second messengers from passive electrical conductance is empirically challenging due to lack

112   of pharmacological or genetic tools. The second messengers, including Ca^{2+} and IP_3 that can

113   move passively via gap junctions [22,23,25,35,36], are involved in intercellular communication via

114   a spatiotemporal spread of coordinated oscillations in gap-junction coupled networks

115   [22,23,25,35–37] and can increase the GSW frequency [38]. Yet, it is not clear whether their

116   intercellular gap junction permeabilities can enable regenerative movement from the leading to

117   the trailing ICCs to entrain cells and thus facilitate propagation of the slow-wave [8,18].

118   Our objectives were therefore to first develop a computational framework which includes

119   constitutive stomach wall cells, biophysical models of the cells, gap junctions through which

120   electrical coupling exists, second messenger exchange across gap junctions, and modulation of

121   second messenger concentration by an endogenous enteric neural stimulus. Second, we utilized

122   this framework to assess the contribution of intercellular electrical coupling and intercellular

123   exchange of second messengers on longitudinal entrainment of the gastric slow-wave.

124   To develop a computational framework, we created a gastric motility network (GMN). We modeled

125   realistic cell models for ICCs incorporating the intrinsic mechanisms for pacemaker potential

126   generation (or oscillatory) activity. To enable inter-ICC coordination, we modeled electrical

127   coupling and second messenger (IP$_3$ and Ca^{2+}) exchange between adjacent cells in a chain. Each

128   ICC was also coupled to an SM cell, forming a pacemaker unit. The membrane voltage and period

129   (or frequency) of the SM cells were used to assess network entrainment, as in empirical studies.

130   Further, we set a rostrocaudal gradient for the enteric neural stimulus input to the ICCs along the

131   ICC chain.

132   Since enteric neural stimulation influences the intracellular second messenger concentration, we

133   first evaluated the importance of a gradient in the stimulus along the chain for development of a

134   caudally propagating gastric slow-wave. We hypothesized that a linear gradient would enable

135   gastric slow-wave propagation along the chain. Next, we examined whether exchange of second

136   messengers alone can generate propagation of the gastric slow-wave. We hypothesized that

137   addition of exchange of second messengers to electrical coupling would enhance the length of

138   the oscillator chain over which entrainment is preserved (referred to as *entrainment range*

139   hereafter). When the oscillators spanning the rostral end of the chain to the caudal end of the

140   chain are entrained, we refer to the phenomena as rostrocaudal entrainment and if the entrained

141   region spans a certain length from the rostral end, but falls short of the caudal end, we considered

142   it partial entrainment. We also assessed how changing electrical coupling strength and second

143   messenger permeability influenced the pacemaker potential frequency and the time for the slow-

144   wave to propagate from the rostral to the caudal end of the stomach, i.e. the velocity of the slow-

145   wave. We hypothesized that systematic increase in coupling strengths would both increase the

146   pacemaker potential frequency and reduce the time taken for gastric slow-wave propagation.

147   Finally, we hypothesized that variability in coupling strengths from cell-to-cell would not disrupt

148   longitudinal entrainment if both electrical coupling and second messenger exchange mechanisms

149   are present.

150   A novel computational framework with both pacemaker and muscle cells that includes intercellular

151   exchange of second messengers and where the pacemakers receive a neural stimulus was

152   developed to simulate and understand propagation of the slow-wave in the stomach. The results

153   indicate that a gradient of neural modulation along the ICCs is necessary for gastric slow-wave

154   propagation and its presence controls the directionality of the propagating slow-wave in an

155   entrained network. Although intercellular exchange of second messengers is not necessary for

156   slow-wave propagation, its presence can enhance the rostrocaudal length of the stomach over

157   which entrainment is preserved and, in its absence, the entrainment range is compromised (partial

158   entrainment is observed). This compromise is reflected by signs of decoupled slow waves and

159   bradygastria. As hypothesized, on an increase of electrical coupling strength and second

160   messenger permeability, the velocity of slow-wave propagation increased while the pacemaker

161   potential frequency increased with the former and decreased with the latter. Our model with the

162   distinct intercellular mechanisms (exchange of second messengers and electrical coupling) in

163   combination with the intracellular feedback pathways and a rostrocaudal neural stimulus gradient

164   allows SM cells to oscillate with a moderate range of frequencies and the gastric slow-wave to

7

165   propagate with a broad range of velocities. Importantly, in the presence of variability in coupling

166   strengths as would occur in biological networks, the existence of intercellular exchange of IP_3 can

167   preserve the longitudinal entrainment to a greater extent along the length of the stomach and

168   eliminate signs of bradygastria and/or tachygastria. Together these results enhance our

169   understanding of the intrinsic and extrinsic mechanisms engaging second messengers for the

170   propagation of a robust gastric slow-wave essential for normal peristalsis.

171

Results

173   **A biologically realistic gastric motility network (GMN) model for the stomach**

174   To develop a gastric motility network (GMN) model for the stomach, we considered the length of

175   the stomach spanning the mid-corpus to the terminal antrum. The schematic of the stomach in

176   **Fig 1A** highlights the arrangement and diversity of cell-types in the stomach wall [11,12]. We

177   focused on modeling the myenteric ICC and circular muscle layers which are most widely studied

178   experimentally. The computational models for the ICCs and SM cells include a diverse set of

179   biophysical properties reported in these cells [39–41] and are formulated as conductance-based

180   models [42,43]. In the pacemaker ICCs, we incorporated widely accepted pathways for producing

181   intrinsic oscillatory behavior. These included a cytosolic mitochondrial-endoplasmic reticulum

182   (ER)-based Ca^{2+} buffering mechanism, a membrane potential dependent intracellular

183   concentration change in IP_3, and IP_3 receptor mediated Ca^{2+} release from the ER, in addition to

184   the transmembrane voltage-activated ionic currents (see **Equations 3 and 4** in **Methods**) as

185   shown in **Fig 1B** [20,41]. Whereas for the SM cell model, we included a muscle-specific

186   sarcoplasmic-reticular mechanism of Na^+/Ca^{2+} exchange to moderate the intracellular Ca^{2+} in

187   addition to the transmembrane currents as noted in **Fig 1C**. The ionic current equations defining

188   the properties of these cells were derived from published models for the ICCs and SM cells (e.g.,

189   [42,43]) and rely on relevant experimental work for the validity of the underlying model

8

190   assumptions (e.g., [39,40,44]). These cellular features were incorporated in our model to ensure

191   both biological compliance as well as agreement with published computational models (e.g.,

192   [7,19,42,43], see **S1 Table**). Our equations, parameter descriptions, and simulation methods are

193   described in the **Methods** section. The resulting simulated membrane voltage characteristics bear

194   close resemblance to empirical evidence, as shown in **Fig 1D (left,** ICC pacemaker potential**;**

195   **right,** SM cell slow-wave potential**).** The intrinsic frequency of oscillations for both ICCs and SM

196   cells were tuned to ~3.0 cycles per minute to match closely with the membrane potential

197   recordings from the guinea-pig gastric antrum ICCs [5] and the canine antrum SM cells [40]**.**
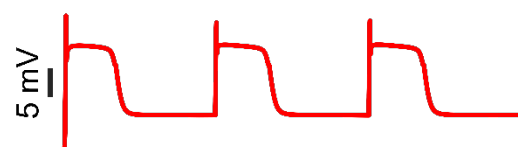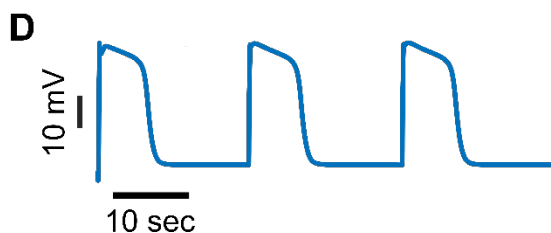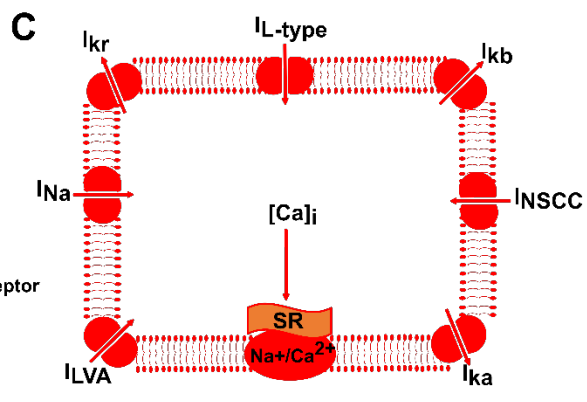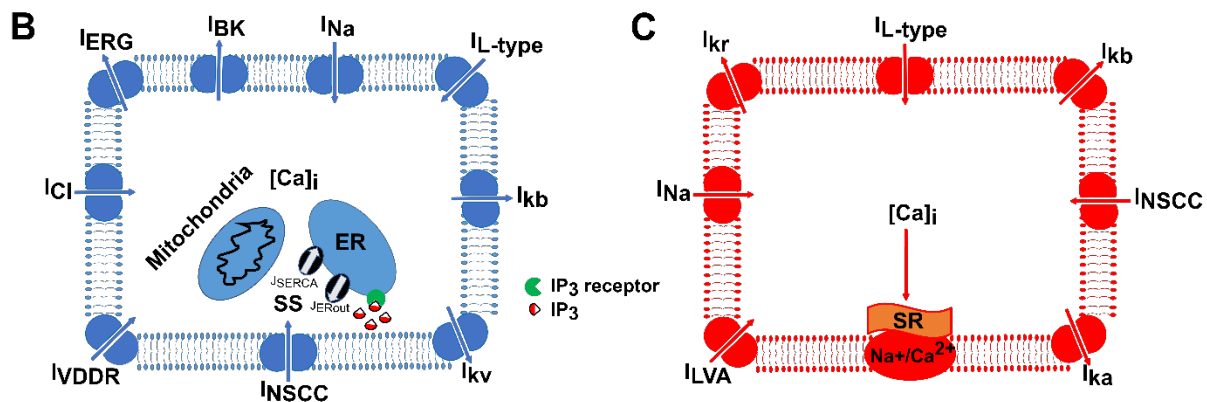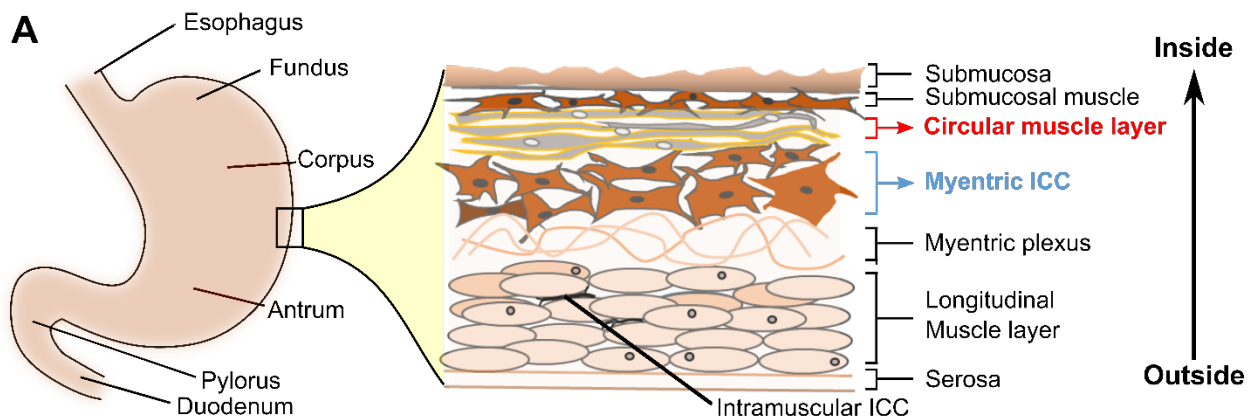
198

199 **Fig 1. Biophysical models for ICCs and SM cells involved in gastric motility.** Schematics showing **(A)**

200 anatomical divisions of the stomach and the arrangement of various cell types in the stomach wall, **(B)**

201 membrane ionic currents and intracellular Ca^{2+}-IP_3 components included in an interstitial cell of Cajal (ICC)

202 model, and **(C)** membrane ionic currents in a smooth muscle (SM) cell model. See **Table 1** for symbols and

203 details of ionic currents. $[Ca]_i$ = Intracellular Ca^{2+}, ER= endoplasmic reticulum, Na^+/Ca^{2+} = Sodium/Calcium

204 exchange pump, SR = Sarcoplasmic reticulum, SS = Submembrane space, **(D)** Simulated rhythmic

205 membrane potential dynamics in an ICC (left panel) and an SM cell (right panel), respectively.

206 The gastric motility network architecture consists of a longitudinal chain of ICCs bordered by a

207 similar inner chain of SM cells, with one-to-one connectivity formed through nearest-neighbor

208 coupling as shown in **Fig 2**; This closely mimics their biological arrangement in the mammalian

209 stomach [14,39,45]. Endogenously ICCs are coupled via gap junctions [15–17] which permit

210 exchange of ions and other small molecules; We therefore incorporated both an electrical

211 conductance and second messenger permeabilities, namely, Ca^{2+} and IP_3, between ICCs [22,23].

212 Between each ICC and its connected SM cell, and between adjacent SM cells we incorporated

213 electrical conductance-based coupling [15]. For the overall network, we incorporated 42 ICCs and

214 42 SM cells formulated using >1500 ODEs and >2000 parameters. As such the network offers a

215 complex, but realistic, framework to evaluate mechanisms involving ICC-ICC, SM-SM, and ICC-

216 SM coupling and their contributions to inter-ICC coordination resulting in the GSW propagation.

217 **Fig 2** highlights the framework used to assess whether and how the intrinsic and extrinsic

218 mechanisms engaging second messengers control the inter-ICC coordination necessary for

219 generation of the GSW and thus, the *entrainment range* in this GMN. The enlarged box inset

220 shows the intracellular pathways of the ICC model essential for its intrinsic oscillatory behavior or

221 pacemaker activity. These consist of the multi-stage feedback pathway between the membrane

222 potential, V_m and the intracellular Ca^{2+} and IP_3 concentrations. The intracellular Ca^{2+} is further

223 divided into two compartments: Ca^{2+} in the sub-space (SS) consisting of the ER and mitochondria

10

224   ($[Ca]_{SS,i}$) and near membrane Ca^{2+} ($[Ca]_i$). The bold arrows in the schematic show the inflows

225   and outflows of the key model variables (see **Table 1** in **Methods** for description of the membrane

226   ion channel currents). The dashed arrows with annotation highlight the positive feedback

227   pathways important for intrinsic pacemaking in the ICC model. Note that the membrane potential

228   exerts a positive feedback on intracellular IP$_3$ concentration (see $V_m - IP_3$ feedback in **Fig 2**,

229   **Equation 4** in **Methods,** also [20,27,41]); The intracellular IP$_3$ concentration, $[IP_3]_i$, in turn affects

230   the $[Ca]_{SS,i}$ concentration through the outward Ca^{2+} flux from the ER (J_{ERout}) [46–48], as

231   highlighted by the $IP_3 - Ca^{2+}$ feedback in **Fig 2**. Lastly, the $[Ca]_{SS,i}$ increases a non-selective

232   cation channel current (NSCC) which closes the loop by impacting the membrane potential (the

233     $Ca^{2+} - V_m$ feedback) [49,50].

234   An initiating event for pacemaker activity (enteric neural stimulus) is assumed to increase the IP$_3$

235   production rate and is modeled as a constant rate, β, for each ICC (see **Equation 4** in **Methods**).

236   Biologically, increases in IP$_3$ levels can originate from endogenous release of neurotransmitters

237   from enteric neurons [26] and subsequent activation of G-protein coupled muscarinic receptors

238   on ICCs at cholinergic synapses along the gastrointestinal (GI) tract [26,51]. In our model, we

239   assume the neurotransmitter release and uptake by receptors as a single event termed as 'enteric

240   neural stimulus'. The enteric neural stimulus driven increase in [IP$_3$] results in an increase in the

241     $[Ca]_{SS,i}$ mimicking the endogenous release of Ca^{2+} from IP$_3$-operated stores in the ER. In

242   response to $[Ca]_{SS,i}$ increase, the Ca^{2+} uniporter on the mitochondrial membrane is gated open,

243   and Ca^{2+} ions flow into the mitochondria down the steep electrochemical gradient (the term J_{Uni}

244   in **Equation 3** in **Methods** represents this mechanism). This is thought to remove a larger number

245   of Ca^{2+} ions from the subspace than had previously entered from the ER, causing a temporary

246   drop in the subspace Ca^{2+} concentration [42,49,50]. This activates the non-selective cation

247   channel current leading to membrane depolarization and onset of oscillation in the ICC.

248   Subsequently, further increase in $[Ca]_i$ due to opening of voltage-dependent Ca^{2+} channels is

249   followed by activation of voltage- and Ca^{2+}-dependent K^+ currents to cause repolarization that

250   restores V_m to hyperpolarized values. The above events repeat to cause the regenerative

251   pacemaker potential activity.

252   To enable longitudinal entrainment of ICCs along the stomach's length with a rostrocaudal

253   frequency gradient we set a rostrocaudal gradient for the enteric neural stimulus (β) that

254   modulates IP_3 production along the ICC chain (see **Fig 2**). Such a gradient reflects evidence that

255   cholinergic inputs to the ICCs show a rostrocaudal decrement along the GI tract [52,53].

256   The overall framework allowed us to examine whether engaging adjacent ICCs via two distinct

257   mechanisms would result in similar entrained slow-wave. One mechanism relies on the electrical

258   conductivity of the gap junction coupling between ICCs which *directly* depolarizes their membrane

259   voltage during entrainment. This is a widely used formalism used in previous modeling studies

260   [7,17]. The second mechanism based on exchange of IP_3 and Ca^{2+} between adjacent ICCs has

261   not been explored in previous models to examine the *entrainment range* (however see [8]). In our

262   GMN model we also assume that exchange of second messengers between ICCs can occur via

263   gap junctions [22–24]; the permeabilities are set for these small molecules (see **Equations 6 and**

264   **7** in **Methods**).
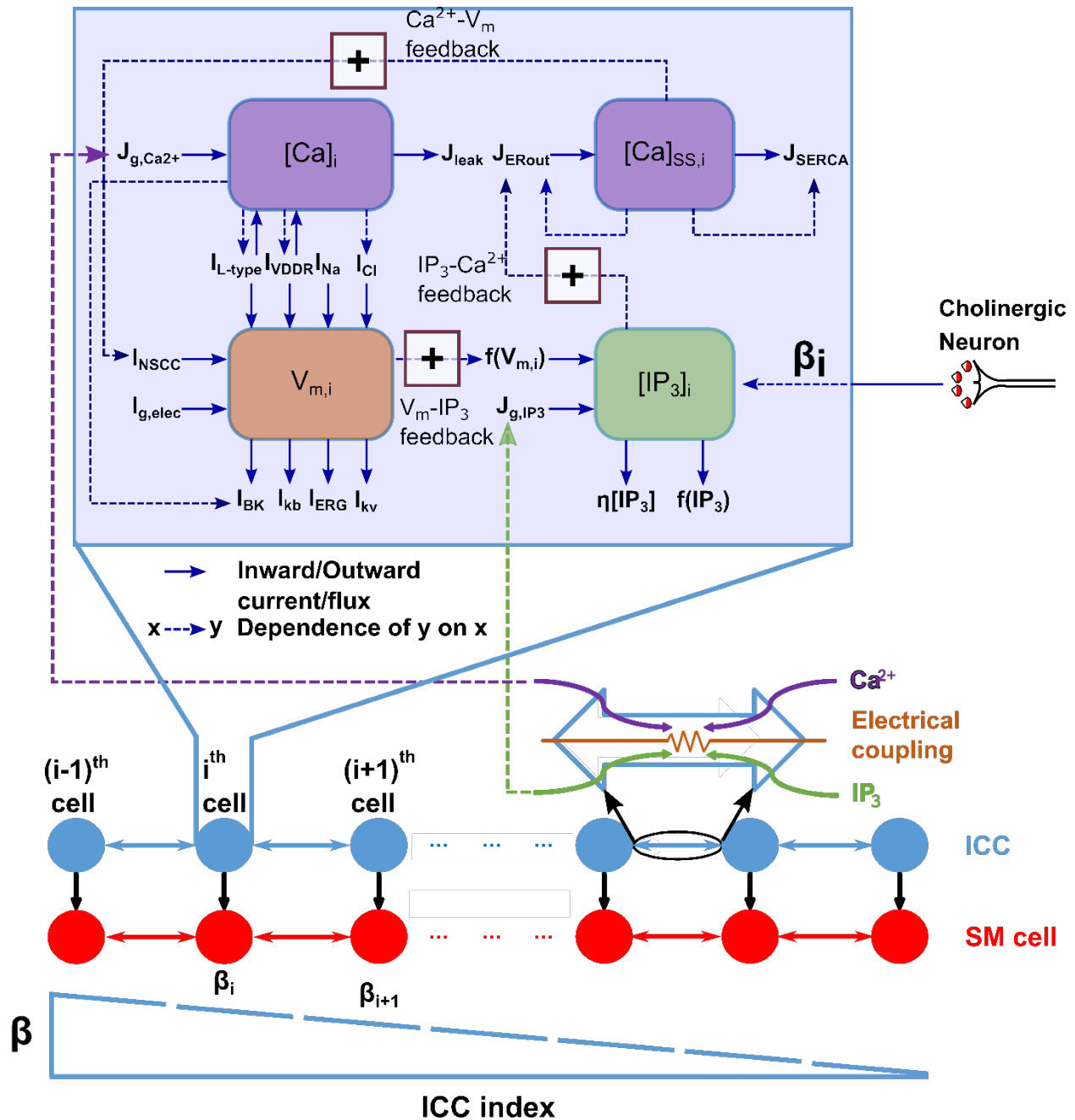
Fig 2. Gastric Motility Network model architecture. The GMN is constituted of a chain of nearest-neighbor coupled interstitial cells of Cajal (ICC) and associated smooth muscle (SM) cells. The ICCs have electrical and second messenger (Ca^{2+} and IP_3) based coupling, while the ICC to SM and SM to SM couplings are only electrical. There is a negative gradient in enteric neural stimulus (β) that modulates IP_3 production rate along the rostrocaudal ICC chain (ICC index). Key variables and their interconnections impacting the functionality of an ICC are illustrated in the enlarged inset. The bold arrows in the inset show

272   the inflows and outflows of key variables. The dashed arrows indicate dependency of the sink variable on

273   the source variable. The dashed arrows with (+) sign highlight the positive feedback pathways important

274   for intrinsic pacemaking by an ICC. See **Table 1** and text for further details.

275   **Longitudinal entrainment of ICCs produces a slow-wave for normal peristalsis**

276   We tested whether the GMN model can produce a slow-wave of uniform frequency similar to a

277   rostrocaudally propagating slow-wave for normal peristalsis in the intact stomach (e.g., in the cat

278   [45], in the dog [39], and guinea pig and humans [14]). We also examined whether the SM cells

279   driven by the entrained ICCs exhibit the expected positive and constant time lags between

280   adjacent cells from the rostral to the caudal end of the network [30,33,45,54]. The ICC/SM pair

281   function as a pacemaker unit. We report the membrane potential of SM cells as a proxy for the

282   pacemaker unit activity (also see **S8 Fig**) as is done in experimental work [45,55].

283   The network was simulated for 900 seconds, where steady-state entrainment was observed

284   approximately after 300 seconds of transient response. **Fig 3** highlights the entrainment and the

285   resulting slow-wave in the GMN at steady-state. In **Fig 3A**, a spatiotemporal map of the

286   membrane potentials of the 42 SM cells demonstrates the rostrocaudal propagation of the slow-

287   wave in the network. The grey shaded regions indicate the up-swing, and the black regions the

288   down-swing in the membrane voltage of the SM cells. A single GSW cycle consists of successive

289   phases of activity from the rostral to the caudal-most pacemaker units. In **Fig 3B**, we highlight the

290   membrane potential of every 7th SM cell in the network. We define and measure *SM Cell Period*

291   as the time between two consecutive peaks in the membrane voltage of an SM cell. An increase

292   or decrease in the *SM Cell Period* reflects bradygastria and tachygastria, respectively. *Relative*

293   *Lag* is defined as the time difference between the peak membrane voltage of SM_1 and SM_i, where

294   *i* = 2,3,4…42, and *Total Lag* as the time between the peak membrane voltages of SM_1 and SM_{42}

295   and. Slow-wave velocity is inversely proportional to the *Total Lag,* provided that the *Total Lag*

296   value reaches a constant value*.* At steady-state, *Relative Lags* should reach constant values

14

297   along the length of the network for a normal slow-wave exhibiting entrainment. Any deviation of

298   *Relative Lag* from constancy reflects decoupling.

299   In our model, at steady-state, the average *SM Cell Period* over 7 slow-wave cycles for the

300   boundary cells SM Cell 1 and SM Cell 42 were 17.7 (± s.d. = 0.01) seconds and 17.7 (± s.d. =

301   0.01) seconds respectively. These periods match closely with those observed *in vitro* in studies

302   of cat [45] and guinea pig stomach SM cells [14]). At steady-state, the computed *Total Lag*

303   reached an approximately constant value of 20.8 (± s.d. 0.02) seconds (**Fig 3C**), and it was

304   consistent between consecutive cycles. The *Relative Lag* for each cell reached an approximately

305   constant value (**Fig 3D**) as well as the periods for all the SM cells in the network (observed from

306   the spatiotemporal map of *SM Cell Periods* in **Fig 3E**). These results indicate the entrainment of

307   all the pacemaker units to a uniform gastric slow-wave frequency.

308   For comparison with empirical results, we also performed meta-analysis of *in vitro* recordings from

309   the cat stomach reported by *Xue S et al.,* [45] and generated the *Relative Lag* and spatiotemporal

310   map of *SM Cell Periods*. These are illustrated as insets in **Fig 3D** and **3E** and corroborate our

311   model findings**.** Thus, we demonstrate that our GMN model is a biologically plausible

312   comprehensive network capable of generating an entrained slow-wave in the stomach with the

313   appropriate rostrocaudal phase lags to support normal peristalsis.
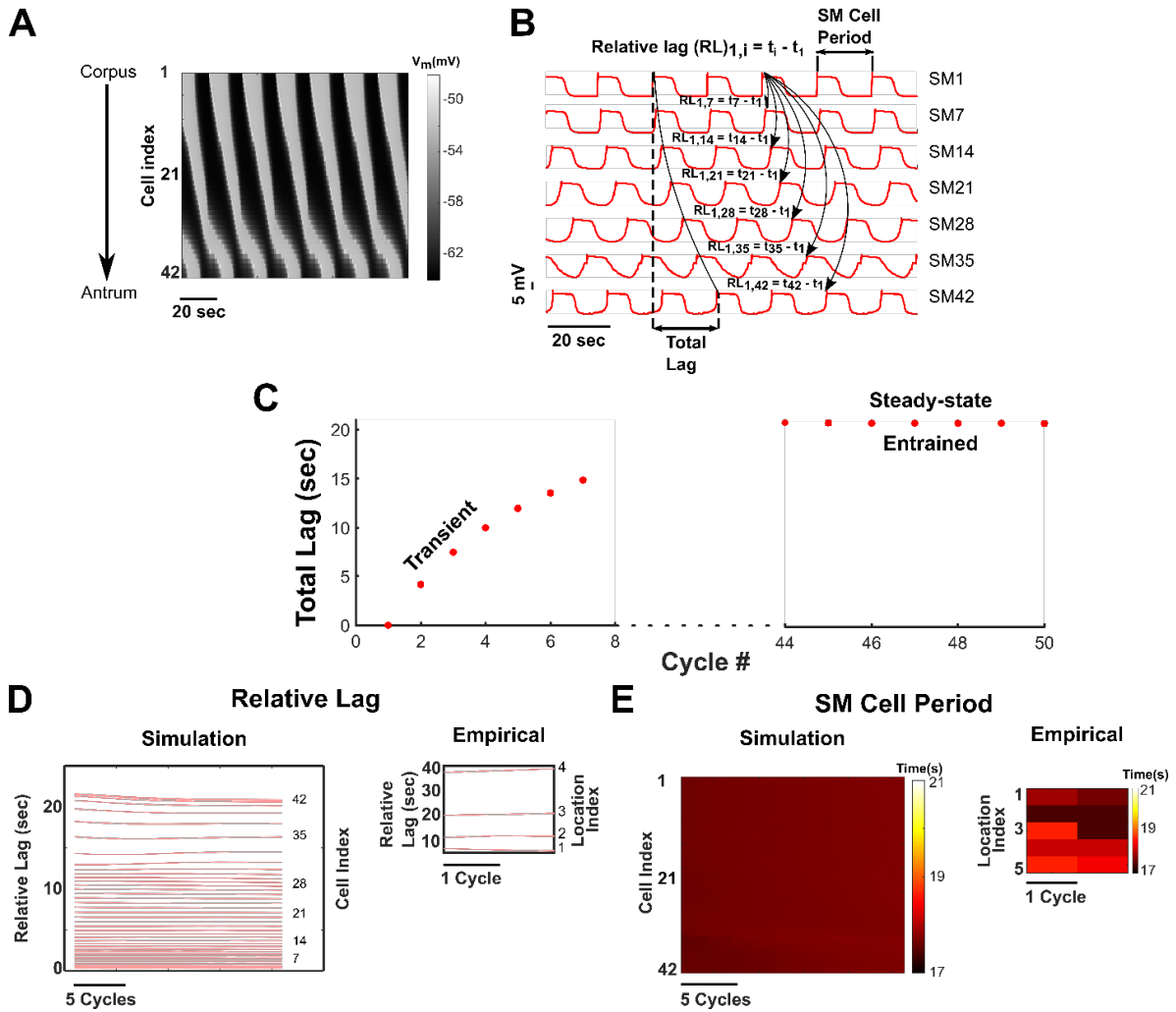
Fig 3. Slow-wave propagation and entrainment in the GMN. (A) Spatiotemporal plot of the SM cell membrane potential along the length of the stomach (vertical axis) and time (horizontal axis) of all 42 SM cells of the network. The direction of slow-wave propagation occurs from the rostral end of the network (representing the mid-corpus) to the caudal end (representing the terminal antrum). **(B)** The membrane potential of 7 equidistant SM cells in the 42-cell network. **(C)** *Total Lag* for the first 7 cycles of simulation and the last 7 cycles of simulation (at steady state). **(D)** *Relative Lag* (RL) between the 1st SM cell and i^{th} SM cell in the network for the last 20 cycles, where i = 2, 3, 4,…, 42. The lag increases from the rostral end of the network to the caudal end, indicating a decrease in slow-wave velocity. **(E)** Spatiotemporal map of periods of all 42 SM cells in the network for the last 20 cycles. The inset plots for the *Relative Lag* (**Fig 3D**) and *SM Cell Period* (**Fig 3E**) were generated from the *in vitro* recordings of SM activity at different locations along the length of the cat stomach [45], where location 1 is the rostral-most recording.

16

326 **Inter-ICC electrical coupling and second messenger exchange synergize to generate**

327 **slow-wave propagation**

328 Our *in silico* model with distinct electrical gap junction conductance and IP$_3$ and Ca^{2+}

329 permeabilities enabled us to study their specific contributions to network entrainment and GSW

330 properties as shown in **Fig 4**. We examined the behavior of the *in silico* GMN model with coupling

331 between ICCs through electrical gap junctions alone (**Fig 4A1**), with coupling through second

332 messenger exchange of Ca^{2+} and IP$_3$ (**Fig 4A2**) alone, or with both (**Fig 4A3**) over 900 seconds

333 (as for the default network in **Fig 3**). When either electrical gap junction coupling or Ca^{2+} and IP$_3$

334 permeabilities alone were present, we observed partial entrainment along the rostrocaudal chain

335 as demonstrated by the *Relative Lags* (**Fig 4B1** and **4B2**) and the *SM Cell Periods* (**Fig 4C1** and

336 **4C2**) and the results with electrical gap junction coupling alone (**Fig 4B1** and **4C1**) were akin to

337 those observed in motility disorders where slow waves are decoupled and bradygastria is

338 observed in the antrum while the corpus continues to demonstrate normal electrical activity [56].

339 However, when both constitutive mechanisms were activated simultaneously, an enhanced

340 *entrainment range* (**Fig 4A3, 4B3** and **4C3**) was obtained suggesting that addition of exchange

341 of second messengers to electrical coupling has a synergistic effect.
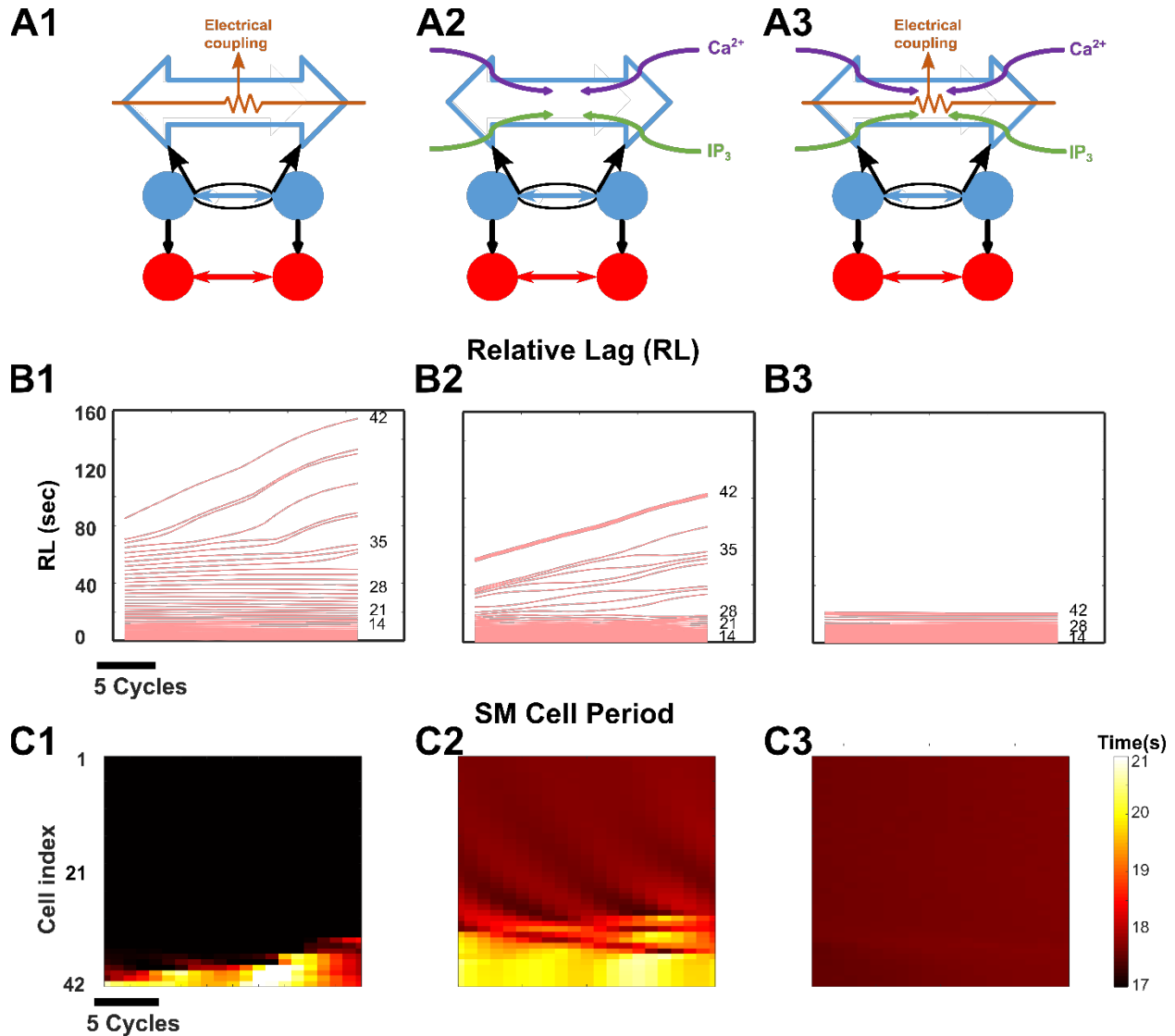
Fig 4. Enhanced longitudinal entrainment. Synergy of electrical coupling and second messenger exchange preserve longitudinal entrainment along the entire length of the stomach. (A1, A2 and A3) Structure of the network, when only electrical coupling is present **(A1)**, when only exchange of second messengers is present **(A2),** and when both electrical coupling and exchange of second messengers are present **(A3)**. **(B)** The *Relative Lags* for the three different cases shown in **Fig 4A** are measured from the last 20 cycles of respective simulations. **(C)** Spatiotemporal maps of *SM Cell Periods* in the three different cases respectively.

18

350 **Impact of increasing strengths of electrical gap junction coupling and exchange of**

351 **second messengers between ICCs**

352 We performed a sensitivity analysis to characterize the effects of increasing strengths of electrical

353 conductivity versus second-messenger permeabilities in inter-ICC coupling on network

354 entrainment and found that they influence the entrainment range, the gastric slow-wave velocity,

355 and the pacemaking frequency. **Fig 5A-5C illustrate** the network's behavior for increasing inter-

356 ICC electrical coupling conductance, $G_{ICC-ICC}$ two times above and below a default value of 0.7

357 nS. The spatiotemporal maps of SM cell membrane potential and the corresponding *Relative Lag*

358 and action potential periods of SM cells are respectively shown for the lowest (**Fig 5B1-5B3, left**)

359 and highest (**Fig 5B1-5B3, right**) $G_{ICC-ICC}$ values considered. In this range of coupling

360 conductance strengths, the network transitioned from partial entrainment (**Fig 5B1-5B3, left**) to

361 complete rostrocaudal entrainment (**Fig 5B1-5B3, right**). For the lowest $G_{ICC-ICC}$ value

362 considered, the *Relative Lag* diagram illustrated in **Fig 5B2, left** shows decoupled slow waves,

363 whereas the *SM Cell Period* diagram depicted in **Fig 5B3, left** demonstrates signs of bradygastria.

364 Steady-state rostrocaudal entrainment was achieved only for higher values of the $G_{ICC-ICC}$ as

365 shown by the levelling out of *Total Lag* in the color-coded insets in **Fig 5C**. Overall, an increase

366 in the strength of electrical coupling conductance produced an enhancement in the *entrainment*

367 *range*.

368 **Fig 5E-5G** present the network outcome for increasing IP$_3$ permeability (values of P_{IP3} two times

369 above and below a default value of 8.0 sec^{-1}) at the default value for the electrical coupling

370 conductance. The spatiotemporal maps of SM cell membrane potential and the corresponding

371 *Relative Lag* and action potential periods of SM cells are shown for the lowest (**Fig 5F1-5F3, left**)

372 and highest (**Fig 5F1-5F3, right**) P_{IP3} values considered. Similar to increasing $G_{ICC-ICC}$ values,

373 the networks with increasing P_{IP3} values demonstrated a transition from partial entrainment to

374 complete rostrocaudal entrainment. For the lowest P_{IP3} value considered, the network generates

375   decoupled slow waves as shown in the *Relative Lag* diagram of **Fig 5F2, left**; however, unlike

376   lowest $G_{ICC-ICC}$ value, the network having lowest P_{IP3} value considered demonstrates signs of

377   tachygastria as illustrated by the *SM Cell Period* diagram in **Fig 5F3, left**. The tachygastria can

378   be prevented by increasing exchange of IP_3 across ICCs (**Fig 5F3, right**) [57].

379   For increasing $G_{ICC-ICC}$ and P_{IP3}, in both cases, the effect on *Total Lag* was qualitatively similar,

380   i.e., decreased with increasing coupling strengths and reached an asymptote as shown in **Fig**

381   **5D1 and 5H1** (actual values are provided in **S2, S4 Tables** respectively). These results suggest

382   that increasing inter-ICC coupling strengths leads to robust rostrocaudal network entrainment

383   wherein the gastric slow-wave velocity approaches a limit.

384   However, $G_{ICC-ICC}$ and P_{IP3} increases differentially altered the *SM Cell Periods* in the entrained

385   networks at steady-state. This is shown in **Fig 5D2** and **Fig 5H2** respectively (actual values in **S3**

386   and **S5 Tables**). The *SM Cell Period* decreased with increasing $G_{ICC-ICC}$, whereas increasing

387   values of P_{IP3} increased the *SM Cell Period*. These results suggest that with an increase in P_{IP3},

388   a decrease in the pacemaking frequency occurs whereas the gastric slow-wave velocity

389   increases. Collectively, the results suggest that on an increase of electrical coupling strength and

390   IP_3 permeability, the velocity of gastric slow-wave propagation increased while the pacemaker

391   potential frequency increased with the former and decreased with the latter.

392   We also exclusively increased the Ca^{2+} permeability (P_{Ca2+}) to test its effects on network

393   entrainment. We noted that even two orders of magnitude changes above and below the default

394   value of P_{Ca2+} produced negligible effect on all the network characteristics analyzed: *entrainment*

395   *range*, *Relative Lag*, *SM Cell Periods* and *Total Lag* in the entrained networks (see **S6 Fig**). This

396   is likely due to an order of magnitude lower permeability of Ca^{2+} compared to IP_3 for gap junctions

397   [18]. Due to this lack of effect of P_{Ca2+} on entrainment and gastric slow-wave characteristics, in

398   what follows, we will only focus on changing P_{IP3}.

399

21
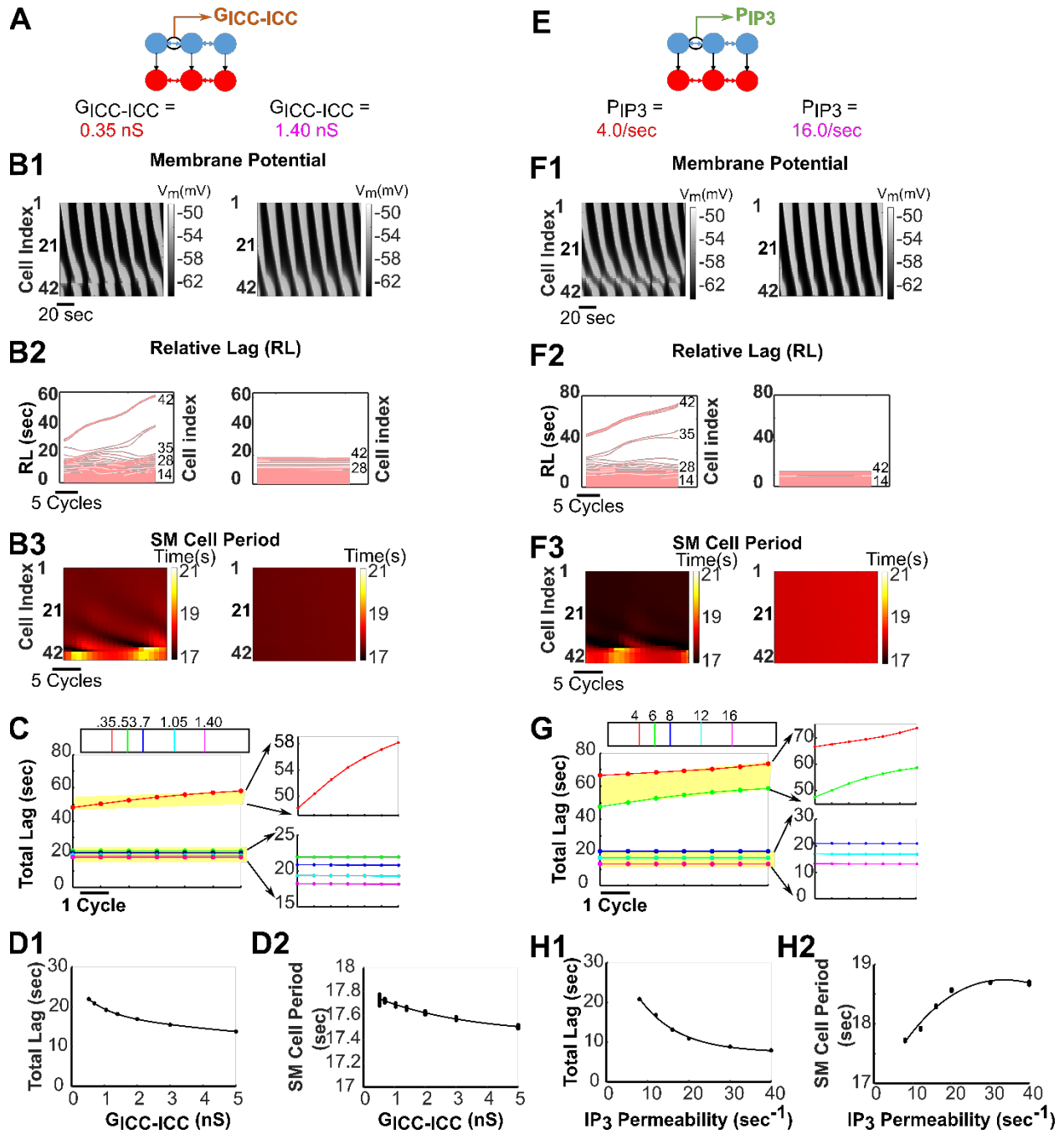
400 **Fig 5. Electrical gap junction and second messenger coupling strengths. The inter-ICC coupling**

401 **strengths impact GMN entrainment, gastric slow-wave velocity and pacemaker frequency. (A, E)**

402 $G_{ICC-ICC}$ and P_{IP3} are altered for the simulations in **Fig 5B-5D** and **Fig 5F-5H**, respectively. **(B)**

403 Spatiotemporal map of membrane potential **(B1),** *Relative Lags* **(B2),** and spatiotemporal map of *SM Cell*

404 *Periods* **(B3)** for the network when $G_{ICC-ICC}$ = 0.35 nS (left panels, partially entrained) and 1.4 nS (right

405 panels , entrained). **(C)** The *Total Lag* for changes in $G_{ICC-ICC}$ is shown for the last 7 cycles of 900-sec

406 simulations for different conductance values (nS) indicated by the color legend. The two distinct classes of

407 responses are enlarged in the right panels (lower ones entrained, upper ones partially entrained). An

408 increase in *Total Lag* indicates decrease in slow-wave velocity. **(F)** Spatiotemporal maps of membrane

409 potential **(F1),** *Relative Lags* **(F2),** and spatiotemporal maps of *SM Cell Periods* **(F3)** for the network when

410 P_{IP3} = 4.0 sec^{-1} (left panels, partially entrained) and 16.0 sec^{-1} (right panels, entrained). **(G)** The *Total Lag*

411 for changes in P_{IP3} is shown for the last 7 cycles of 900-sec simulations for different conductance values

412 (nS) indicated by the color legend. **(D, H)** For several networks, the mean *Total Lag* (odd numbered panels)

413 and the *SM Cell Period* (even numbered panels) of the last 7 cycles for each network with respect to its

414 $G_{ICC-ICC}$ and P_{IP3} can be fit by individual exponential function, respectively. For increasing values of $G_{ICC-ICC}$,

415 an exponential fit ($y = a_1 e^{-x/\beta_1} + a_2 e^{-x/\beta_2}$, where a_1 = 8.65, β_1 = 0.75, a_2 = 18.23, β_2 = 17.87) has been

416 drawn along the mean value of *Total Lag* and for increasing values of P_{IP3}, another exponential fit ($y =$

417 $a_1 e^{-x/\beta_1} + a_2 e^{-x/\beta_2}$, where a_1 = 7.44, β_1 = 1.70e5, a_2 = 32.07, β_2 = 9.37) has been drawn along the mean

418 values of *Total Lag*. Partially entrained networks have not been considered for equation fitting. For *SM Cell*

419 *Period* calculation, the last cell (42nd cell) has been considered as the representative cell of the network.

420 An increase in *Total Lag* indicates decrease in slow-wave velocity while a decrease in *SM Cell Period*

421 indicates increase in pacemaking frequency.

422 **Inter-ICC IP$_3$ exchange preserves longitudinal entrainment**
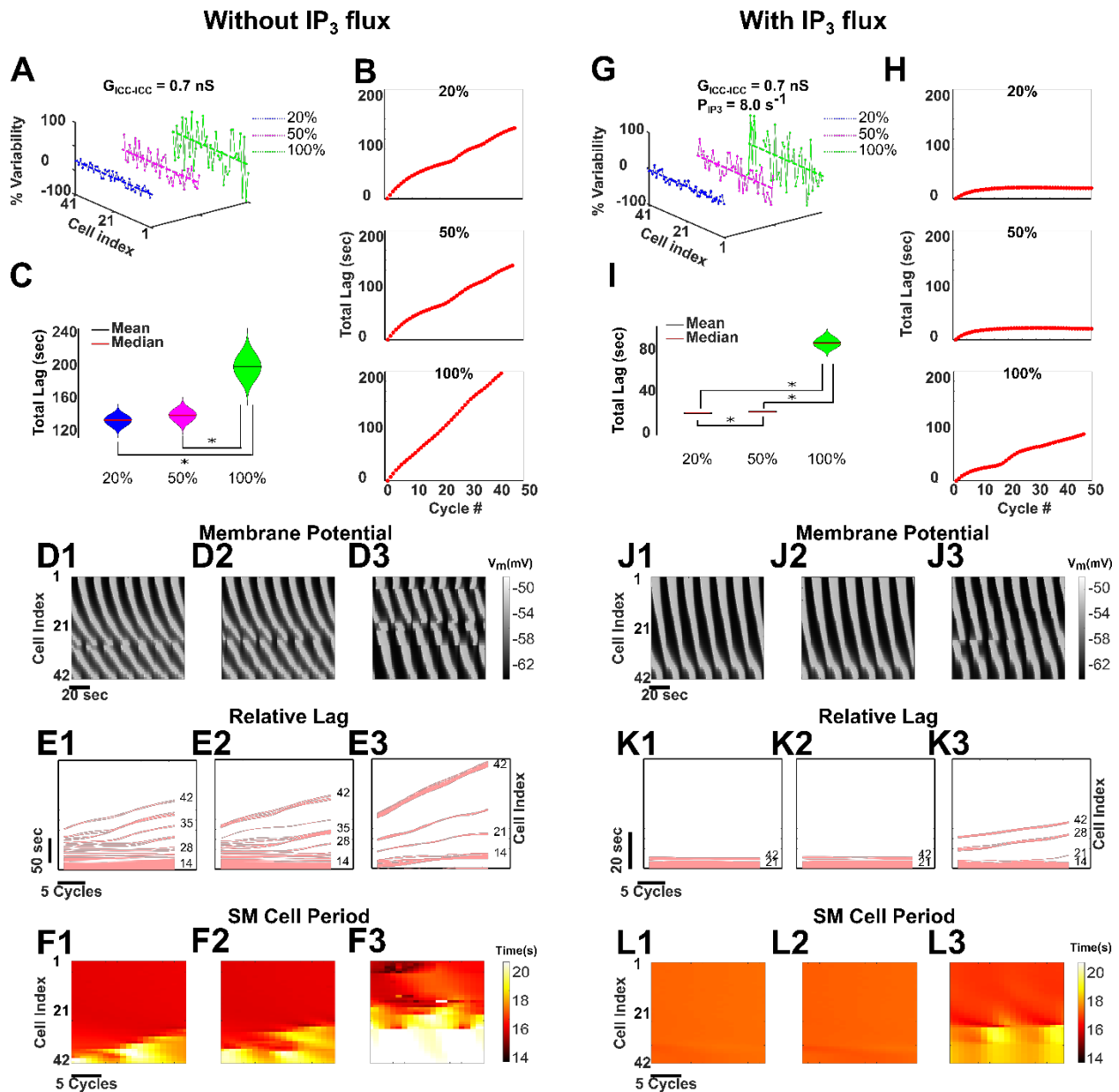
423 Variability in ICC coupling strengths could stem from variable gap junction densities in the

424 stomach [58,59]. We find that inter-ICC IP$_3$ ensures appropriate slow-wave propagation and

425 stable pacemaking potential generation under variable ICC coupling strengths. We first introduced

426 variability in coupling conductance by random sampling of $G_{ICC-ICC}$ values from a uniform

427 distribution (see corresponding results in **Fig 6A-6F**) in the absence of inter-ICC IP$_3$ exchange.

428 The range of conductance values were $default \pm 20\%$ or $\pm 50\%$ or $\pm 100\%$ (see **Fig 6A**). As

429 shown in **Fig 6B**, the *Total Lags* have not reached a steady-state value in any of the three

430 networks. Consequently, slow-wave velocity cannot be inferred from here and the failure of *Total*

431 *Lag* to attain a constant value indicates absence of rostrocaudal network entrainment. **Fig 6C**

432 shows the distribution of *Total Lags* computed over the last 7 cycles of simulation, using violin

433 plots. From these plots we note that the variability in *Total Lags* consistently increases with the

434 variability in coupling conductance strength. The SM cell membrane potential (**Fig 6D**), *Relative*

435 *Lag*, (**Fig 6E**) and *Period* (**Fig 6F**) indicate that variability of $G_{ICC-ICC}$ indeed gave rise to clusters

436 of partial entrainment. The *Relative Lag* diagrams in **Fig 6E**, in particular, provide evidence for

437 the decoupled slow waves. The *SM Cell Period* diagrams in **Fig 6F1 and 6F2** bears close

438 resemblance to bradygastria whereas **Fig 6F3** demonstrates a mix of bradygastria and

439 tachygastria. These results suggest that, in the absence of inter-ICC IP$_3$ exchange, decoupled

440 slow waves and bradygastria and/or tachygstria can coexist.

441 Next, we included the inter-ICC IP$_3$ exchange along with electrical coupling and varied both the

442 $G_{ICC-ICC}$ and P_{IP3} values 20%, 50%, and 100% about their corresponding default values of 0.7 nS

443 and 8.0 sec^{-1}, respectively (**Fig 6G**). Interestingly, addition of IP$_3$ exchange enabled rostrocaudal

444 entrainment for networks with 20% and 50% variability in these coupling parameters, but not with

445 100% variability (see panels in **Fig 6H**). The distribution of *Total Lags* in **Fig 6I**, the SM cell

446 membrane potential (**Fig 6J**), *Relative Lag* (**Fig 6K**), and *Period* (**Fig 6L**) further confirms these

447 results. The *Relative Lag* diagrams in **Fig 6K1 and 6K2** show absence of decoupling for 20% and

448 50% variability, respectively; in contrast, for 100% variability, **Fig 6K3** shows decoupled slow

449 waves as evidenced by temporal changes in *Relative Lag*. Parallel observations have been made

450 from the *SM Cell Period* diagrams in **Fig 6L1 and 6L2**, where signs of abnormal rhythmicity

451 (bradyagastria or tachygstria) are effectively eliminated, although for 100% variability, there are

452   still signs of bradygastria (**Fig 6L3**). Furthermore, **Fig 6H** demonstrates that there is no substantial

453   difference in the latency to reach entrainment between the networks having 20% and 50%

454   variability. Together these results suggest that the existence of intercellular exchange of IP$_3$ can

455   preserve the longitudinal entrainment to a greater extent along the length of the stomach, thereby

456   preventing decoupling and restoring the normal behavior.

457

458

24

459 **Fig 6. Entrainment in GMN is resilient to variability in inter-ICC coupling strengths. (A,G)** The

460 variability in only $G_{ICC-ICC}$ (**A**) and both $G_{ICC-ICC}$ and P_{IP3} (**G**) (20%, 50%, and 100% variability) are shown

461 around their mean values. **(B, H)** *Total Lag* of the network without inter-ICC IP₃ exchange for three different

462 variabilities in $G_{ICC-ICC}$ **(B)** and of the network with inter-ICC IP₃ exchange for three different variabilities in

463 $G_{ICC-ICC}$ and P_{IP3} **(H).** The latency to entrainment cannot be inferred from any of the panels in **(B)**, since

464 the *Total Lag* has not reached steady-state value in any of them. However, the latency to entrainment can

465 be measured from the first two panels in **(H)**, since the *Total Lag* has attained constant value in these two

466 cases. **(C, I)** *Total Lag* is shown for each case for the last 7 cycles in steady-state. A violin plot shows the

467 differences in *Total Lag* for all three cases. The asterisk (*) symbol represents a statistically significant

468 difference between the corresponding quantities. Spatiotemporal diagrams of membrane potential **(D, J)**,

469 *Relative Lags*, **(E, K)** and spatiotemporal maps of *SM Cell Periods* **(F, L)** for the network are shown for

470 three different variabilities in $G_{ICC-ICC}$ for the network without inter-ICC IP₃ exchange and in $G_{ICC-ICC}$ and

471 P_{IP3} for the network without inter-ICC IP₃ exchange, respectively.

472

Discussion

473

474 We have developed a computational framework consisting of a novel non-linear mathematical

475 model for slow-wave propagation in the stomach wall that includes physiologically established

476 intra- and intercellular mechanisms. Utilizing this framework, we have assessed the contribution

477 of intercellular electrical coupling and intercellular exchange of second messengers on

478 longitudinal entrainment of the gastric slow-wave. The intracellular concentrations of Ca²⁺ and IP₃

479 are modulated by intercellular exchange of respective molecules (see **Equations 2 and 4**). We

480 found that our model with dynamically coupled nonlinear oscillators fed with second messengers

481 from intercellular exchange and enteric neural stimuli, can regulate the frequency of contractions

482 and velocity of the slow-wave, and can enhance the range of longitudinal entrainment of the

483 gastric slow-wave. The combination of electrical coupling and exchange of second messengers

484 provides robustness to the *entrainment range* in the presence of biological variability. In summary,

485 our detailed analyses of the ICC coupling mechanisms reveal ways in which the constitutive gap

486 junction coupling mechanisms can enhance the network range and stability of the gastric slow-

487 wave essential for peristaltic movement of food and fluid. Furthermore, this model can be used to

488 examine novel hypotheses concerning aberrant mechanisms that may underlie different motility

489 disorders.

490 **Development of Gastric Motility Network (GMN) model**

491 In the present study, we developed a computational model consisting of a longitudinal

492 arrangement of biophysically based ICC and SM cells found in the stomach wall. Since ICCs and

493 their network are regarded as the key players for generation of pacemaker potentials and

494 propagation of slow waves, we investigated whether and how the intrinsic properties of ICCs that

495 are also modulated by enteric neural inputs enable inter-ICC coordination essential for

496 entrainment. We also examined the crucial intercellular pathways that influence the *entrainment*

497 *range*, important for long distance GSW propagation necessary for normal peristalsis. For this,

498 we considered multiple interacting feedback pathways involving the intracellular key variables

499 such as membrane potential, Ca^{2+} and IP_3 concentration of an ICC as well as intercellular

500 electrical coupling and exchange of second messengers. Further based on corroborative

501 evidence that enteric neuron inputs to ICCs show a rostrocaudal gradient [52,53], and indirect

502 evidence that indicates that neurotransmitters enhance IP_3 in a variety of pacemaker cells [27–

503 29], we assumed a gradient in the enteric neural stimulus along the ICC chain. Such a gradient

504 was essential for the rostrocaudal entrainment of the slow-wave as also demonstrated in previous

505 computational models [7,19].

506 **Control of slow-wave characteristics by inter-ICC IP_3 exchange**

507 First, our simulation results for single ICC and SM cells agree qualitatively and semi-quantitatively

508 with the experimentally measured results (**Fig 1**), thus validating the GMN model components.

509 Next, our results show that the GMN with its multi-stage feedback between IP_3-Ca^{2+}-V_m combined

26

510   with the intercellular pathways (**Fig 2**) can generate slow-wave propagation with a uniform

511   frequency and a uniform rostrocaudal lag, i.e., entrainment (**Fig 3**). Particularly, the presence of

512   inter-ICC IP_3 exchange in addition to the gap junction electrical conductance can increase the

513   range of longitudinal entrainment (**Fig 4**), while simultaneously minimizing the signs of

514   bradygastric decoupled slow waves. Our observations are in accordance with the suggestion that

515   bradygastria can potentially result from a failure of normal entrainment [60]. While the distinct

516   intercellular mechanisms modeled in our network (exchange of second messengers and electrical

517   coupling) are experimentally inseparable, the biophysical formulation included in the GMN model

518   allowed examination of their individual contributions to longitudinal entrainment of ICCs. Second,

519   we systematically evaluated the network behavior for increasing values of electrical conductance

520   and IP_3 permeability (since Ca^{2+} permeability was shown to have little to no impact on GSW

521   entrainment). Surprisingly, the IP_3 exchange affected the features of the slow-wave in a manner

522   that can stabilize the propagating wave (from tachygastric decoupled slow waves for low IP_3 to a

523   normal coupled gastric slow-wave for elevated IP_3). In particular, increased IP_3 permeability of

524   gap junctions resulted in an *increase* in the *SM Cell Period* (bordering the signs of bradygastria)

525   whereas increased gap junction electrical conductance caused a *decrease* in the *SM Cell Period*

526   (bordering the signs of tachygastria). Thus, in combination with the contrasting effects of electrical

527   conductivity, the IP_3 coupling could flexibly modulate the SM cell frequencies. We suggest that

528   the apparent compensatory effect of IP_3 permeability could act as a brake on preventing runaway

529   tachygastria (elevated SM cell frequencies, which is inversely related to *SM Cell Period* or

530   pacemaking potential duration) in the event of increasing electrical coupling strengths. Increased

531   gap junction density, which is reflected by increased gap junction coupling strength in our model,

532   has been demonstrated in colonocytes during bacterial infections resulting in diarrhea generation

533   [61]. Whether the same holds true for gastric motility disorders requires further experimental

534   investigation. Even if the electrical gap junction density becomes exceedingly high, the inter-ICC

27

535   IP$_3$ coupling makes sure that the SM cell frequency, and therefore, gastric contraction frequency

536   stays in a physiologically plausible range.

537   Interestingly, increasing values of electrical conductance or IP$_3$ permeability led to an increased

538   slow-wave velocity. In our results, the increase of slow-wave velocity was demonstrated by a

539   decrease in the *Total Lag* of the slow-wave (**Fig 5**). These observations are very similar to the

540   observations in studies of the dog small intestine where a negative gradient of gap junctions exists

541   across the duodenum, jejunum and ileum and so does the slow-wave velocity in these

542   compartments of the small intestine [62]. Electrophysiological experiments with gap junction

543   enhancers (such as in Rotigaptide [63]) also support the observations of our computational study.

544   As per our knowledge, such gap junction enhancers have not been employed as medicinal

545   interventions yet, although they have the potential to elevate the reduced slow-wave velocity as

546   observed in gastroparesis patients [60]. We would have to be very cautious though in introducing

547   such enhancers, since slow-wave velocity has been reported to be already highly elevated in the

548   gastric corpus of aged patients having gastroparesis with impaired peristalsis [64] and somewhat

549   elevated in glucagon induced hyperglycemic dogs [6]. Future experiments could investigate the

550   proper dosage of the gap junction enhancers so that the slow-wave velocity remains in a moderate

551   range. For now, we can only speculate that in an intact stomach, the electrical gap junction

552   coupling strength probably does not reach an exceedingly high value, and even if it has a

553   moderately high value, **Fig 5D1 and 5H1** show that the slow-wave velocity reaches a limit, which

554   is within a physiologically reasonable range.

555   **Distinct period-velocity relationships exist for increasing $G_{ICC-ICC}$ and P_{IP3}**

556   According to coupled oscillator theory, the direction of the slow-wave would depend on the

557   frequency gradient of component pacemaker ICCs, whereas the slow-wave velocity would

558   depend on the intercellular coupling strength [65]. Therefore, ideally, there should be a dispersion

559   relationship between slow-wave velocity and frequency (expressed by *SM Cell Period*, in our

28

560   case). However, previous studies of the canine gastric antrum [65] and porcine gastric corpus

561   and antrum [66] suggest a dependence of slow-wave velocity on the observed *SM Cell Period*.

562   The period-velocity relationship as noted in **Fig 5H1 and 5H2** (higher the period, higher the

563   velocity) for increasing permeability of IP_3 supports these *in vitro* [65] and *in vivo* [66] findings. In

564   contrast, the period-velocity relationship noted in **Fig 5D1 and 5D2** (lower the period, higher the

565   velocity) for increasing electrical coupling strength is somewhat surprising. Because, if the period

566   decreases, the velocity of a slow-wave should drop as a response to encroachment on the tail of

567   the previous slow-wave (see **Fig 7 in [66]** for a more intuitive understanding). Although such a

568   relationship has been observed along the length of the intestine [62] under normal conditions, its

569   occurrence is probably due to the emergence of frequency plateaus, which in fact reflect localized

570   decoupling due to the reduced gap junction density at certain points along the intestinal length

571   [59]. Frequency plateaus are not observed in the stomach under normal conditions.

572   Consequently, localized decoupling due to the reduced gap junction density along the length of

573   the stomach is an unlikely explanation for the observed period-velocity relations in **Fig 5D1 and**

574   **5D2**. We believe that the less pronounced effect of increasing $G_{ICC-ICC}$ on velocity (reflected as

575   *Total Lag* in **Fig 5D1**) and period (illustrated in **Fig 5D2)** compared to the effect of increasing P_{IP3}

576   on the same quantities (**Fig 5H1 and 5H2**) makes sure that the trajectory of a slow-wave having

577   increased $G_{ICC-ICC}$ does not appear synchronously with the tail of the previous slow-wave, thus

578   avoiding the positive correlation between period and velocity. In our model results, we are

579   concerned only with the velocity from the rostral end to the caudal end. Measurement of velocity

580   gradient (if there is any) and a non-uniform modeling of gap junction conductance [15] along with

581   the measurement of gap junction density in various animal models could shed further light on the

582   model predictions.

583 **Exchange of second messengers ensures robust rostrocaudal entrainment when**

584 **biological variability is present**

585 Finally, we showed that while variability in electrical coupling results in loss of rostrocaudal

586 entrainment (signs of bradygastria and mix of bradygastria and tachygastria observed), presence

587 of IP$_3$ exchange despite variability in its permeability, can restore rostrocaudal entrainment (**Fig**

588 **6**) and therefore, is essential for peristalsis. Here, inter-ICC IP$_3$ exchange offers resilience to the

589 increased variability in coupling strength. This is noteworthy because gap junctions in ICC

590 networks can have variable density in different compartments of the stomach [15,16] and the

591 observed consequences of increasing the variability in inter-ICC coupling in our simulations

592 highlight that this might be a feature important for regulating the wave velocity while maintaining

593 the range of entrainment. Our model with the distinct intercellular mechanisms (exchange of

594 second messengers and electrical coupling) in combination with the intracellular feedback

595 pathways and rostrocaudal neural stimulus gradient allows SM cells to oscillate with a moderate

596 range of frequencies and the gastric slow-wave to propagate with a broad range of velocities (**Fig**

597 **5**). Thus, the GMN confers high robustness to the rostrocaudal entrainment of ICCs, including

598 under instances of biological variability in coupling pathways (**Fig 6**). Robustness is a fundamental

599 property of evolvable complex biological systems [67]; a simple mechanism cannot handle

600 extreme changes in physical quantities. Our model offers a new integrative framework for

601 conceptualizing GSW propagation and regulation as a robust system of dynamically coupled

602 oscillators fed with second messengers through intercellular exchange.

603 **Biological and theoretical assumptions of the GMN model**

604 Although numerous biological mechanisms are involved in the orchestration of gastric motility

605 [68], it is well-established that the peristaltic movement of food/liquid is mediated by a propagating

606 wave of smooth muscle contractions along the stomach wall [5,13,14,69]. This so-called gastric

607 slow-wave involves electrical activity transmitted aborally within the SM cells [55,70]. However,

30

608   the SM cells on their own cannot produce such a regenerative wave [70,71]. The regenerative

609   electrical activity responsible for the GSW is known to originate largely in the intrinsic pacemaker

610   ICCs [5,42]. Different sets of ICCs innervate circular and longitudinal muscle cells (e.g., myenteric

611   ICCs, intramuscular ICCs [5,13]) and all ICCs may not contribute similarly to pacemaker potential

612   generation and GSW propagation [68]. Our ICC cell model is derived primarily from experimental

613   work on myenteric ICCs, which are widely accepted as intrinsic pacemakers involved in the

614   generation of the pacemaker potential required for GSW propagation [5]. We incorporated known

615   membrane properties in the ICCs and SM cell models using the conductance-based formalism

616   and hand-tuned the conductance parameters to match experimental voltage recordings in these

617   cells (**Fig 1C and 1D**) [45]. Although our model can reproduce rather accurately the established

618   properties of a gastric slow-wave, it should be noted that the description of the underlying

619   mechanisms is by no means exhaustive. For example, we have chosen to use a Hodgkin-Huxley

620   formalism for the ion currents whereas Markovian models would allow for a more detailed

621   description of the complex kinetics of processes (activation, deactivation, inactivation, and

622   recovery from inactivation) that the channels exhibit. However, it can be very challenging to meet

623   the information requirements for defining the transitional rate constants of a Markovian model, in

624   addition to higher computational processing demands [72].

625   Although ICCs are intrinsic pacemakers, the GSW can significantly be impacted by the coupling

626   between them [8,73,74]. Gap junctions are well-established pathways for such coupling [75]. The

627   gap junctions carry various ions and molecules. Some of these (e.g., K^+) are passively conducted

628   due to the voltage gradients between adjacent cells (the electrical component), while others

629   spread when there are periodic depolarizations in ICCs that generate these molecules in

630   abundance. The latter are typically second messengers such as IP_3 and Ca^{2+}, which involve

631   chemical coupling via connexin channels [22,23,25,35,36]. The diameter of gap junctional pores

632   allows a wide enough path for Ca^{2+} and IP_3 to move across the cells through gap junction

31

633   connexins [76]. To model electrical coupling, a simple ohmic conductance has been widely

634   assumed by previous modeling studies [7,8,19,69,77,78], supported by findings that pacemaker

635   current generated in ICCs is transmitted to the SM cells by gap junction channels located between

636   the ICCs and SM cells [15,17]. We additionally assumed a distinct exchange of second

637   messenger (Ca^{2+} and IP_3) between adjacent ICCs. Second messenger exchanges are modeled

638   in such a way that they enable Ca^{2+} induced Ca^{2+} release and IP_3 induced IP_3 release. Although

639   Ca^{2+} induced Ca^{2+} release is a widely assumed phenomenon within a biological cell, IP_3 induced

640   IP_3 release has also been suggested as a plausible event [79]. Ca^{2+} permeability was set an order

641   of magnitude lower than that of IP_3 permeability. This assumption was based on the fact that the

642   range of diffusion of IP_3 is orders of magnitude higher compared to free Ca^{2+} (24 µm compared

643   to 0.1 µm). IP_3 also degrades much more slowly than free Ca^{2+} (1 sec vs. 0.00003 sec) [80].

644   Previous modeling studies of intercellular Ca^{2+} waves in astrocytes [35] and smooth muscle cells

645   [24] support this approach of modeling Ca^{2+} and IP_3 permeability. The exchange of IP_3 was

646   modeled as proportional to the IP_3 concentration gradient between adjacent cells (see **Methods,**

647   also [81]). Although IP_3 can diffuse within the cell cytoplasm and not necessarily through the gap

648   junctions, we assumed that IP_3 only moves to the adjacent cells based on the concentration

649   gradient. For **Fig 3-5**, we considered constant values of gap junction coupling parameters and for

650   **Fig 6**, we assumed uniform distribution of gap junction coupling strength, which resembles the

651   gap junction density. Because of the scarcity of data regarding gap junction distribution, we limited

652   our simulations to only uniform distribution.

653   In a chain of intrinsic pacemakers, oscillators have their own distinct intrinsic frequency. In an

654   arbitrarily long chain of oscillators, entrainment can emerge provided there exists a linear

655   frequency gradient with fixed frequency difference between the ends [82]. Interestingly in the

656   stomach (also throughout the GI tract), it is known that there is a rostrocaudal frequency gradient

657   in the ICC pacemaker cells. Although such gradients may be achieved by numerous intrinsic and

32

658   network mechanisms [7,19], we assume that such a gradient in intrinsic frequencies can be

659   achieved due to a maintained gradient in [IP_3] production rate. Presently it is unclear what sets

660   this gradient tone in IP_3 production rate. One possibility could be IP_3 produced by activation of

661   muscarinic receptors due to graded distribution of cholinergic neuron inputs in different functional

662   compartments of the GI tract [52,53]. Although peristalsis can occur even without the help of

663   neural excitation [68], under most circumstances, the enteric nervous system, provides excitation

664   of the musculature required for the stomach wall contraction [26,83], primarily via ICCs. Enteric

665   neurons located in the Myenteric Plexus preferentially directly influence ICCs through

666   neurotransmitters released at synapses which then connect to muscle cells via gap junctions.

667   Since ICCs are closer to the nerve terminal endings and have the muscarinic receptors (M2 and

668   M3) that are responsive to the neurotransmitters, the effect of the Myenteric neurons on ICCs is

669   more important (much smaller gap for neurotransmitters to diffuse) than the direct link to the SM

670   cells (far away and with lesser innervation). Acetylcholine, the primary neurotransmitter released

671   from enteric neurons, is broken down by Acetylcholine esterase, thus preventing it from reaching

672   receptors on SM cells. Consequently, we considered the enteric neural stimulus (β) to act

673   exclusively on ICCs in our GMN model. The animal models that lack ICCs with muscarinic

674   receptors show that there is little or no cholinergic response in SM cells because Acetylcholine is

675   broken down before it can be taken up by receptors on SM cells [26]. In our model, we maintained

676   a linear gradient of β to ensure that rostral ICCs successively entrained caudal ICCs. This way,

677   we assembled a chain of realistic ICCs which show a rostrocaudal gradient in their intrinsic

678   frequencies like that observed in the stomach. In the heart, fast-pacing sinoatrial node cells

679   entrain the slow-pacing atrioventricular node cells [84], like what is observed in an intact stomach.

680   Besides being intrinsic pacemakers, ICCs are also involved in neurotransmission, setting the

681   membrane potential of SM cells, and in stretch sensing [51]. Future experiments examining

682   effects of neural input on ICCs may shed further light on the neural contribution to pacemaker

683   potential generation and slow-wave propagation. Empirical measurements of the neural stimulus

33

684   on ICCs at different points along the stomach would strengthen the validity of our model, offering

685   further hypotheses for the mechanisms underlying genesis of functional and pathological slow

686   waves in the stomach. The mathematical modeling framework outlined in our study is a step in

687   this direction and provides an exploration testbed for precise modulation of intra/intercellular

688   pathways to examine their role in the above-mentioned phenomena.

689

Methods

690

691   The model network of ICC-SM cells is described in **Fig 2**. The network consists of 42 ICCs and

692   42 SM cells implemented and simulated in MATLAB 2019a (Mathworks.inc). Together, the

693   extensive biological details of ICC and SM cell physiology and the assumed intercellular coupling

694   resulted in a large network model with 1554 nonlinear differential equations (23 for each ICC and

695   14 for each SM cell) consisting of over 1000 parameters. The parameter values were chosen from

696   published models [7,42,43].

697   **ICC cell model**

698   We adopted a well-described conductance-based model by Corrias *et al.*, 2008 [42] for the ICCs

699   (also see [7,19]). The rate of change in the membrane potential, V_{ICC}, for each ICC is as follows:

700
$$C_{m,ICC} \frac{dV_{ICC}}{dt} = -\left(\sum I_{ion,ICC} + I_{g,ICC}\right),$$
(1)

701   where V_{ICC} is the ICC membrane potential, $C_{m,ICC}$ is the ICC membrane capacitance, $I_{ion,ICC}$

702   represents the summation of all the ionic currents in ICC, and $I_{g,ICC}$ represents the current through

703   the gap junctions between the ICCs. The different ionic currents included in the model are

704   described in **Table 1.** The dynamics of the voltage-dependent gating variables for the ionic

705   currents follow the well-known Hodgkin-Huxley formalism, where each current is represented by

706   a battery (electrochemical driving force) in series with a variable resistance and the cell membrane

707   as a capacitor in parallel. The combined actions of these ion channel currents reproduce the three

708   phases of a gastric action potential: depolarization, plateau phase, and repolarization. Detailed

709   descriptions of these ionic currents are provided in the github repository

710   (https://github.com/ashfaq-polit/Slow_waves_in_the_stomach) and are based on previous

711   modeling studies [42,43,85].

712   **Table 1: Ionic currents in the ICC model**

Symbol used	Description	Symbol used	Description
I_{L-type}	L-type Ca^{2+} current	I_{NSCC}	Non-selective cation current
I_{VDDR}	Voltage-dependent and dihydropyridine-resistant Ca^{2+} current	I_{LVA}	Low voltage-activated Ca^{2+} current
I_{Na}	Voltage-dependent Na^+ current	I_{Cl}	Voltage-dependent chloride current
I_{kv}	Kv1.1-type voltage-dependent K^+ current	I_{kr}	Delayed rectifier K^+ current
I_{ERG}	Ether-a-go-go (ERG) K^+ channel current	I_{ka}	A-type potassium current
I_{kb}	Background K^+ current	I_{coup}	Gap junction current between ICC and SM cell
I_{BK}	Large conductance Calcium-dependent K^+ current		

713

Ca^{2+}-IP$_3$ dynamics in ICCs

715   The equation guiding the intracellular Ca^{2+} dynamics is modeled similar to Fall and Keizer [86]

716   as follows:

717
$$\frac{d[Ca^{2+}]_i}{dt} = f_c \left(\frac{-I_{L-type} - I_{VDDR}}{FV_{cyto}} + J_{leak} - J_{PMCA} + J_{g,Ca^{2+}} \right), \qquad (2)$$

718   Where I_{L-type} and I_{VDDR} are described in Table 1, J_{leak} is a leakage flux between the pacemaker

719   region and the cytosol, J_{PMCA} is the Ca^{2+} flux through the plasmalemmal Ca^{2+} pump, F is the

720   Faraday constant, f_c is a dimensionless constant, V_{cyto} represents the cytosolic volume fraction

721   within the ICC, and $J_{g,Ca^{2+}}$ is the Ca^{2+} flux due to inter-ICC coupling (see **Equation 6**).

722   The Ca^{2+} flux in a sub-membrane space triggered by IP$_3$-operated stores in the endoplasmic

723   reticulum (ER) is important for initiating a gastric action potential. The Ca^{2+} concentration in the

724   sub-membrane space is modeled by the following equation:

725
$$\frac{d[Ca^{2+}]_{PU}}{dt} = f_c \left((J_{NaCa} - J_{Uni}) \frac{V_{mito}}{V_{SS}} + (J_{ERout} - J_{SERCA}) \frac{V_{ER}}{V_{SS}} - J_{leak} \frac{V_{cyto}}{V_{SS}} \right), \qquad (3)$$

726   Where J_{NaCa} and J_{Uni} represent mitochondrial Ca^{2+} fluxes, J_{ERout} and J_{SERCA} represent outward

727   Ca^{2+} fluxes from the ER and inward Ca^{2+} fluxes through the ER. V_{mito}, V_{ER}, and V_{SS} represent the

728   volume fractions for the mitochondria, endoplasmic reticulum, and pacemaker submembrane

729   space, respectively.

730   Increases in intracellular IP$_3$ concentration in each ICC are assumed to depend on: 1) voltage-

731   dependent IP$_3$ increase, 2) inter-ICC coupling-dependent IP$_3$ increase, and 3) neurotransmitter-

732   induced IP$_3$ increase, whereas linear and non-linear degradation of IP$_3$ decrease its concentration.

733   Based on these assumptions, the rate of change in IP$_3$ concentration is given as follows:

734
$$\frac{d[IP_3]}{dt} = P_{MV} \left(1 - \frac{V_m^8}{k_v^8 + V_m^8} \right) - \eta[IP3] - V_{m4} \frac{[IP_3]^4}{k_4^4 + [IP_3]^4} + \beta + J_{g,IP3} , \qquad (4)$$

735   where P_{MV} is maximal rate of voltage-dependent IP$_3$ synthesis, K_V is the half-saturation constant

736   for voltage-dependent IP$_3$ synthesis, η is the rate constant for linear IP$_3$ degradation, V_{m4} is

737   maximal value for the nonlinear IP$_3$ degradation, K_4 is half-saturation constant for the nonlinear

738   IP$_3$ degradation, β represents an enteric neural stimulus that modulates IP$_3$ production, and $J_{g,IP3}$

739   is the IP$_3$ flux due to inter-ICC coupling (see **Equation 7**).

740   **Intercellular coupling between ICCs**

741   Adjacent ICCs are assumed to be coupled via gap junctions with electrical conductance for

742   passive ionic movement between cells [17]. The inter-ICC gap junction current is:

743
$$I_{g,ICC} = G \sum_j (V_i - V_j) , \qquad (5)$$

36

744   where i denotes the index for the source ICC and j denotes the index for adjacent ICCs; G

745   represents electrical conductance of gap junctions.

746   **Second messenger exchange between ICCs**

747   An exchange of second messengers, namely, Ca^{2+} and IP_3 can occur via gap junctions [22–

748   24,81]. The flux describing Ca^{2+} exchange between adjacent ICCs is modeled by a term

749     $$J_{g,Ca^{2+}} = -P_{Ca2+} \sum_j([Ca^{2+}]_i - [Ca^{2+}]_j) \qquad (6)$$

750   complementing Equation 2. Here P_{Ca2+} denotes the permeability coefficient for Ca^{2+} and $[Ca^{2+}]_x$

751   are the intracellular concentrations of Ca^{2+} in the corresponding cells where $x = i/j$. The $P_{Ca^{2+}}$

752   value has been taken from a theoretical study done in hepatocytes [87].

753   The inter-ICC IP_3 flux is modeled using a similar formalism:

754     $$J_{g,IP3} = -P_{IP3} \sum_j([IP_3]_i - [IP_3]_j) \qquad (7)$$

755

756   Here P_{IP3} denotes the permeability coefficient for IP_3 and $[IP_3]_x$ are the intracellular concentrations

757   of IP_3 in the corresponding cells where $x = i/j$. An experimentally determined value of P_{IP3} is rare

758   if not non-existent due to the technical difficulties of measuring [IP_3] in tissue preparations. Hence,

759   the permeability values used in model simulations were adjusted similar to [24,35].

760   **SM cell model**

761   The SM cell model was adopted from Corrias *et al.*, 2007 [43]. Like ICCs, the conductance-based

762   rate of change in membrane potential is given as follows:

763     $$C_{m,SM} \frac{dV_{SM}}{dt} = -\left(\sum I_{ion,SM} + I_{g,SM} - I_{coup}\right), \qquad (8)$$

764     $$I_{coup} = g_{coup}(V_{ICC} - V_{SM}), \qquad (9)$$

765   Where V_{SM} is the SM cell membrane potential, $C_{m,SM}$ is the SM cell membrane capacitance, $I_{ion,SM}$

766   represents the summation of all the ionic currents in the SM cell, $I_{g,SM}$ represents the current

37

767   through the gap junctions between the SM cells, and I_{coup} represents the coupling current from

768   ICC to its corresponding SM cell. Although a bidirectional movement of ions can occur via gap

769   junctions, here we assume that during entrainment depolarization spreads unidirectionally from

770   ICC to SM and that V_{ICC} is always more positive than V_{SM} [70]; hence, the coupling current, I_{coup}

771   is present only in **Equation 8**. The various ionic currents necessary to generate the SM action

772   potential are listed in **Table 1.**

773   **Model simulation and analysis**

774   The ICC-SM model network consisting of 42 ICCs and 42 SM cells was implemented and

775   simulated in MATLAB 2019a (Mathworks.inc) using built-in function ODE15s and variable step-

776   size. The total runtime for each simulation was 900 seconds (each simulation lasted

777   approximately 8 hours on an Intel Xeon (R) CPU, 32 GB RAM Desktop computer). The outcome

778   of the network was interpreted from the spatiotemporal membrane potential, *Relative Lag* and

779   *period of SM cells* (explained in **Results** section). Statistical tests (t-test, one-way ANOVA) were

780   performed as required and an α cutoff of 0.05 was chosen for statistical significance.

781

Author Contributions

783   Conceptualization: RJ, MAA. Formal analysis: MAA. Investigation: MAA, SV, RJ. Project

784   administration and Supervision: RJ. Visualization: MAA, SV. Writing of original draft: MAA,

785   Review and Editing: MAA, SV, RJ.

786

References

788   1.   Sanders KM, Koh SD, Ward SM. Interstitial cells of Cajal as pacemakers in the
789   gastrointestinal tract. Annu Rev Physiol. 2006;68: 307–343.
790   doi:10.1146/annurev.physiol.68.040504.094718

791   2.   Coleski R, Hasler WL. Coupling and propagation of normal and dysrhythmic gastric slow

38

792   waves during acute hyperglycaemia in healthy humans. Neurogastroenterol Motil.
793   2009;21. doi:10.1111/j.1365-2982.2008.01235.x

794 3. Lin X, Chen JDZ. Abnormal gastric slow waves in patients with functional dyspepsia
795   assessed by multichannel electrogastrography. Am J Physiol - Gastrointest Liver Physiol.
796   2001;280: 1370–1375. doi:10.1152/ajpgi.2001.280.6.g1370

797 4. Jebbink RJA, Samsom M, Bruijs PPM, Bravenboer B, Akkermans LMA, Vanberge-
798   Henegouwen GP, et al. Hyperglycemia induces abnormalities of gastric myoelectrical
799   activity in patients with type I diabetes mellitus. Gastroenterology. 1994;107: 1390–1397.
800   doi:10.1016/0016-5085(94)90541-X

801 5. Hirst GDS, Edwards FR. Generation of slow waves in the antral region of guinea-pig
802   stomach - A stochastic process. J Physiol. 2001;535: 165–180. doi:10.1111/j.1469-
803   7793.2001.00165.x

804 6. Du P, O'Grady G, Paskaranandavadivel N, Tang SJ, Abell T, Cheng LK. High-resolution
805   Mapping of Hyperglycemia-induced Gastric Slow Wave Dysrhythmias. J
806   Neurogastroenterol Motil. 2019;25: 276–285. doi:10.5056/jnm18192

807 7. Du P, O'Grady G, Gibbons SJ, Yassi R, Lees-Green R, Farrugia G, et al. Tissue-specific
808   mathematical models of slow wave entrainment in wild-type and 5-HT2B knockout mice
809   with altered interstitial cells of Cajal networks. Biophys J. 2010;98: 1772–1781.
810   doi:10.1016/j.bpj.2010.01.009

811 8. van Helden DF, Imtiaz MS. Ca2+ phase waves: A basis for cellular pacemaking and
812   longrange synchronicity in the guinea-pig gastric pylorus. J Physiol. 2003;548: 271–296.
813   doi:10.1113/jphysiol.2002.033720

814 9. Cheng LK, Komuro R, Austin TM, Buist ML, Pullan AJ. Anatomically realistic multiscale
815   models of normal and abnormal gastrointestinal electrical activity. World J Gastroenterol.
816   2007;13: 1378–1383. doi:10.3748/wjg.v13.i9.1378

817 10. O'Grady G, Egbuji JU, Du P, Lammers WJEP, Cheng LK, Windsor JA, et al. High-
818   resolution spatial analysis of slow wave initiation and conduction in porcine gastric
819   dysrhythmia. Neurogastroenterol Motil. 2011;23: 345–355. doi:10.1111/j.1365-
820   2982.2011.01739.x

821 11. Mandal UK, Chatterjee B, Senjoti FG. Gastro-retentive drug delivery systems and their in
822   vivo success: A recent update. Asian J Pharm Sci. 2016;11: 575–584.
823   doi:https://doi.org/10.1016/j.ajps.2016.04.007

824 12. Camborová P, Hubka P, Sulková I, Hulín I. The pacemaker activity of interstitial cells of
825   Cajal and gastric electrical activity. Physiol Res. 2003;52: 275—284. Available:
826   http://europepmc.org/abstract/MED/12790758

827 13. Hirst GDS, Beckett EAH, Sanders KM, Ward SM. Regional variation in contribution of
828   myenteric and intramuscular interstitial cells of Cajal to generation of slow waves in
829   mouse gastric antrum. J Physiol. 2002;540: 1003–1012.
830   doi:10.1113/jphysiol.2001.013672

831 14. Hirst GDS, Edwards FR. Electrical events underlying organized myogenic contractions of
832   the guinea pig stomach. J Physiol. 2006;576: 659–665. doi:10.1113/jphysiol.2006.116491

833 15. Seki K, Komuro T. Distribution of interstitial cells of Cajal and gap junction protein, Cx 43
834   in the stomach of wild-type and W/Wv mutant mice. Anat Embryol (Berl). 2002;206: 57–
835   65. doi:10.1007/s00429-002-0279-0

836 16. Komuro T, Seki K, Horiguchi K. Ultrastructural characterization of the interstitial cells of
837   Cajal. Archives of Histology and Cytology. 1999. pp. 295–316. doi:10.1679/aohc.62.295

838 17. Cousins HM, Edwards FR, Hickey H, Hill CE, Hirst GDS. Electrical coupling between the
839   myenteric interstitial cells of Cajal and adjacent muscle layers in the guinea-pig gastric
840   antrum. J Physiol. 2003;550: 829–844. doi:10.1113/jphysiol.2003.042176

841 18. Imtiaz MS, Von Der Weid PY, Van Helden DF. Synchronization of Ca2+ oscillations: A
842   coupled oscillator-based mechanism in smooth muscle. FEBS J. 2010;277: 278–285.
843   doi:10.1111/j.1742-4658.2009.07437.x

844 19. Buist ML, Corrias A, Poh YC. A model of slow wave propagation and entrainment along
845   the stomach. Ann Biomed Eng. 2010;38: 3022–3030. doi:10.1007/s10439-010-0051-1

846 20. Van Helden DF, Imtiaz MS, Nurgaliyeva K, Von Der Weid PY, Dosen PJ. Role of calcium
847   stores and membrane voltage in the generation of slow wave action potentials in guinea-
848   pig gastric pylorus. J Physiol. 2000;524: 245–265. doi:10.1111/j.1469-7793.2000.00245.x

849 21. Radebold K, Horakova E, Gloeckner J, Ortega G, Spray DC, Vieweger H, et al. Gap
850   junctional channels regulate acid secretion in the mammalian gastric gland. J Membr Biol.
851   2001;183: 147–153. doi:10.1007/s00232-001-0062-9

852 22. Clair C, Chalumeau C, Tordjmann T, Poggioli J, Erneux C, Dupont G, et al. Investigation
853   of the roles of Ca2+ and InsP3 diffusion in the coordination of Ca2+ signals between
854   connected hepatocytes. J Cell Sci. 2001;114: 1999–2007.

855 23. Carter TD, Chen XY, Carlile G, Kalapothakis E, Ogden D, Evans WH. Porcine aortic
856   endothelial gap junctions: Identification and permeation by caged InsP3. J Cell Sci.
857   1996;109: 1765–1773.

858 24. Koenigsberger M, Sauser R, Lamboley M, Bény JL, Meister JJ. Ca2+ dynamics in a
859   population of smooth muscle cells: Modeling the recruitment and synchronization.
860   Biophys J. 2004;87: 92–104. doi:10.1529/biophysj.103.037853

861 25. Isakson BE, Ramos SI, Duling BR. Ca2+ and inositol 1,4,5-trisphosphate-mediated
862   signaling across the myoendothelial junction. Circ Res. 2007;100: 246–254.
863   doi:10.1161/01.RES.0000257744.23795.93

864 26. Ward SM, Sanders KM. Interstitial cells of Cajal: Primary targets of enteric motor
865   innervation. Anat Rec. 2001;262: 125–135. doi:10.1002/1097-
866   0185(20010101)262:1<125::AID-AR1017>3.0.CO;2-I

867 27. Poggioli J, Sulpice JC, Vassort G. Inositol phosphate production following α1-adrenergic,
868   muscarinic or electrical stimulation in isolated rat heart. FEBS Lett. 1986;206: 292–298.

869   doi:10.1016/0014-5793(86)80999-1

870   28.   Canonico PL, Jarvis WD, Angela Sortino M, Scapagnini U, MacLeod RM. Cholinergic
871   stimulation of inositol phosphate production in cultured anterior pituitary cells.
872   Neuroendocrinology. 1987;46: 306–311. doi:10.1159/000124837

873   29.   Macara B, Gião-T. Rico JM. Effect of Ca2+ modulators on acetylcholine-induced phasic
874   and tonic contractions and A23187-induced contractions in ileal longitudinal muscle and
875   IP3 production. Eur J Pharmacol. 1992;218: 27–33. doi:10.1016/0014-2999(92)90143-R

876   30.   Cohen AH, Holmes PJ, Rand RH. The nature of the coupling between segmental
877   oscillators of the lamprey spinal generator for locomotion: A mathematical model. J Math
878   Biol. 1982;13: 345–369. doi:10.1007/BF00276069

879   31.   Kopell N, Ermentrout GB. Coupled oscillators and the design of central pattern
880   generators. Math Biosci. 1988;90: 87–109. doi:https://doi.org/10.1016/0025-
881   5564(88)90059-4

882   32.   Winfree AT. Biological rhythms and the behavior of populations of coupled oscillators. J
883   Theor Biol. 1967;16: 15–42. doi:https://doi.org/10.1016/0022-5193(67)90051-3

884   33.   Strogatz SH, Stewart I. Coupled oscillators and biological synchronization. Sci Am.
885   1993;269: 102–109. doi:10.1038/scientificamerican1293-102

886   34.   Roenneberg T, Dragovic Z, Merrow M. Demasking biological oscillators: Properties and
887   principles of entrainment exemplified by the Neurospora circadian clock. Proc Natl Acad
888   Sci U S A. 2005;102: 7742–7747. doi:10.1073/pnas.0501884102

889   35.   Ullah G, Jung P, Cornell-Bell AH. Anti-phase calcium oscillations in astrocytes via inositol
890   (1, 4, 5)-trisphosphate regeneration. Cell Calcium. 2006;39: 197–208.
891   doi:10.1016/j.ceca.2005.10.009

892   36.   Sneyd J, Wetton BTR, Charles AC, Sanderson MJ. Intercellular calcium waves mediated
893   by diffusion of inositol trisphosphate: A two-dimensional model. Am J Physiol - Cell
894   Physiol. 1995;268: 537–545. doi:10.1152/ajpcell.1995.268.6.c1537

895   37.   Valiunas V, White TW. Connexin43 and connexin50 channels exhibit different
896   permeability to the second messenger inositol triphosphate. Sci Rep. 2020;10: 1–10.
897   doi:10.1038/s41598-020-65761-z

898   38.   Malysz J, Donnelly G, Huizinga JD. Regulation of slow wave frequency by IP3-sensitive
899   calcium release in the murine small intestine. Am J Physiol - Gastrointest Liver Physiol.
900   2001;280: 439–448. doi:10.1152/ajpgi.2001.280.3.g439

901   39.   el-Sharkawy TY, Morgan KG, Szurszewski JH. Intracellular electrical activity of canine
902   and human gastric smooth muscle. J Physiol. 1978;279: 291–307.
903   doi:10.1113/jphysiol.1978.sp012345

904   40.   Ward SM, Dixon RE, De Faoite A, Sanders KM. Voltage-dependent calcium entry
905   underlies propagation of slow waves in canine gastric antrum. J Physiol. 2004;561: 793–
906   810. doi:10.1113/jphysiol.2004.076067

41. Imtiaz MS, Smith DW, Van Helden DF. A theoretical model of slow wave regulation using voltage-dependent synthesis of inositol 1,4,5-trisphosphate. Biophys J. 2002;83: 1877–1890. doi:10.1016/S0006-3495(02)73952-0

42. Corrias A, Buist ML. Quantitative cellular description of gastric slow wave activity. Am J Physiol - Gastrointest Liver Physiol. 2008;294. doi:10.1152/ajpgi.00528.2007

43. Corrias A, Buist ML. A quantitative model of gastric smooth muscle cellular activation. Ann Biomed Eng. 2007;35: 1595–1607. doi:10.1007/s10439-007-9324-8

44. Du P, Li S, O'Grady G, Cheng LK, Pullan AJ, Chen JDZ. Effects of electrical stimulation on isolated rodent gastric smooth muscle cells evaluated via a joint computational simulation and experimental approach. Am J Physiol - Gastrointest Liver Physiol. 2009;297: 672–680. doi:10.1152/ajpgi.00149.2009

45. XUE S, VALDEZ DT, TREMBLAY L, COLLMAN PI, DIAMANT NE. Electrical slow wave activity of the cat stomach: its frequency gradient and the effect of indomethacin. Neurogastroenterol Motil. 1995;7: 157–167. doi:10.1111/j.1365-2982.1995.tb00221.x

46. De Young GW, Keizer J. A single-pool inositol 1,4,5-trisphosphate-receptor-based model for agonist-stimulated oscillations in Ca2+ concentration. Proc Natl Acad Sci. 1992;89: 9895 LP – 9899. doi:10.1073/pnas.89.20.9895

47. Watras J, Bezprozvanny I, Ehrlich BE. Inositol 1,4,5-trisphosphate-gated channels in cerebellum: Presence of multiple conductance states. J Neurosci. 1991;11: 3239–3245. doi:10.1523/jneurosci.11-10-03239.1991

48. Li Y-X, Rinzel J. Equations for InsP3 Receptor-mediated [Ca2+]i Oscillations Derived from a Detailed Kinetic Model: A Hodgkin-Huxley Like Formalism. J Theor Biol. 1994;166: 461–473. doi:https://doi.org/10.1006/jtbi.1994.1041

49. Takeda Y, Koh SD, Sanders KM, Ward SM. Differential expression of ionic conductances in interstitial cells of Cajal in the murine gastric antrum. J Physiol. 2008;586: 859–873. doi:10.1113/jphysiol.2007.140293

50. Koh SD, Jun JY, Kim TW, Sanders KM. A Ca2+-inhibited non-selective cation conductance contributes to pacemaker currents in mouse interstitial cell of Cajal. J Physiol. 2002;540: 803–814. doi:10.1113/jphysiol.2001.014639

51. Al-Shboul O. The importance of interstitial cells of cajal in the gastrointestinal tract. Saudi J Gastroenterol. 2013;19: 3–15. doi:10.4103/1319-3767.105909

52. Cellini J, DiNovo K, Harlow J, LePard KJ. Regional differences in neostigmine-induced contraction and relaxation of stomach from diabetic guinea pig. Auton Neurosci Basic Clin. 2011;160: 69–81. doi:10.1016/j.autneu.2010.10.006

53. Vanden Berghe P, Coulie B, Tack J, Mawe GM, Schemann M, Janssens J. Neurochemical coding of myenteric neurons in the guinea-pig antrum. Cell Tissue Res. 1999;297: 81–90. doi:10.1007/s004410051335

54. Kelly KA, Code CF, Elveback LR. Patterns of canine gastric electrical activity. Am J

945   Physiol Content. 1969;217: 461–470. doi:10.1152/ajplegacy.1969.217.2.461

946   55.   Hirst GDS, Garcia-Londoño AP, Edwards FR. Propagation of slow waves in the guinea-
947   pig gastric antrum. J Physiol. 2006;571: 165–177. doi:10.1113/jphysiol.2005.100735

948   56.   Kim CH, Azpiroz F, Malagelada JR. Characteristics of spontaneous and drug-induced
949   gastric dysrhythmias in a chronic canine model. Gastroenterology. 1986;90: 421–427.
950   doi:10.1016/0016-5085(86)90942-X

951   57.   You CH, Chey WY. Study of Electromechanical Activity of the Stomach in Humans and in
952   Dogs With Particular Attention to Tachygastria. Gastroenterology. 1984;86: 1460–1468.
953   doi:10.1016/S0016-5085(84)80159-6

954   58.   Venance L, Piomelli D, Glowinski J, Glaume C. Inhibition by anandamide of gap junctions
955   and intercellular calcium signalling in striatal astrocytes. Nature. 1995;376: 590–594.
956   doi:10.1038/376590a0

957   59.   Parsons SP, Huizinga JD. Spatial noise in coupling strength and natural frequency within
958   a pacemaker network; consequences for development of intestinal motor patterns
959   according to a weakly coupled phase oscillator model. Front Neurosci. 2016;10.
960   doi:10.3389/fnins.2016.00019

961   60.   O'Grady G, Angeli TR, Du P, Lahr C, Lammers WJEP, Windsor JA, et al. Abnormal
962   initiation and conduction of slow-wave activity in gastroparesis, defined by high-resolution
963   electrical mapping. Gastroenterology. 2012;143: 589–598.
964   doi:10.1053/j.gastro.2012.05.036

965   61.   Guttman JA, Lin AEJ, Li Y, Bechberger J, Naus CC, Vogl AW, et al. Gap junction
966   hemichannels contribute to the generation of diarrhoea during infectious enteric disease.
967   Gut. 2010;59: 218–226. doi:10.1136/gut.2008.170464

968   62.   Lammers WJEP, Ver Donck L, Schuurkes JAJ, Stephen B. Peripheral pacemakers and
969   patterns of slow wave propagation in the canine small intestine in vivo. Can. Can J
970   Physiol Pharmacol. 2005;83: 1031–1043. doi:10.1139/y05-084

971   63.   Lin X, Zemlin C, Hennan JK, Petersen JS, Veenstra RD. Enhancement of ventricular gap-
972   junction coupling by rotigaptide. Cardiovasc Res. 2008;79: 416–426.
973   doi:10.1093/cvr/cvn100

974   64.   Wang THH, Angeli TR, Ishida S, Du P, Gharibans A, Paskaranandavadivel N, et al. The
975   influence of interstitial cells of Cajal loss and aging on slow wave conduction velocity in
976   the human stomach. Physiol Rep. 2021;8: 1–8. doi:10.14814/phy2.14659

977   65.   Publicover NG, Sanders KM. Myogenic regulation of propagation in gastric smooth
978   muscle. Am J Physiol - Gastrointest Liver Physiol. 1985;11.
979   doi:10.1152/ajpgi.1985.248.5.g512

980   66.   Wang THH, Du P, Angeli TR, Paskaranandavadivel N, Erickson JC, Abell TL, et al.
981   Relationships between gastric slow wave frequency, velocity, and extracellular amplitude
982   studied by a joint experimental-theoretical approach. Neurogastroenterol Motil. 2018;30:
983   1–9. doi:10.1111/nmo.13152

984   67.   Kitano H. Biological robustness. Nat Rev Genet. 2004;5: 826–837. doi:10.1038/nrg1471

985   68.   Huizinga JD, Lammers WJEP. Gut peristalsis is governed by a multitude of cooperating
986   mechanisms. Am J Physiol - Gastrointest Liver Physiol. 2009;296: 1–8.
987   doi:10.1152/ajpgi.90380.2008

988   69.   Edwards FR, Hirst GDS. An electrical analysis of slow wave propagation in the guinea-
989   pig gastric antrum. J Physiol. 2006;571: 179–189. doi:10.1113/jphysiol.2005.100743

990   70.   Suzuki H, Hirst GDS. Regenerative potentials evoked in circular smooth muscle of the
991   antral region of guinea-pig stomach. J Physiol. 1999;517: 563–573. doi:10.1111/j.1469-
992   7793.1999.0563t.x

993   71.   Sanders KM. Rhythmic electrical activity and regulation of gut motility. Eur Rev Med
994   Pharmacol Sci. 2008;12 Suppl 1: 129–131.

995   72.   Fink M, Noble D. Markov models for ion channels: versatility versus identifiability and
996   speed. Philos Trans R Soc A Math Phys Eng Sci. 2009;367: 2161–2179.
997   doi:10.1098/rsta.2008.0301

998   73.   Park KJ, Hennig GW, Lee HT, Spencer NJ, Ward SM, Smith TK, et al. Spatial and
999   temporal mapping of pacemaker activity in interstitial cells of Cajal in mouse ileum in situ.
1000   Am J Physiol - Cell Physiol. 2006;290: 1411–1427. doi:10.1152/ajpcell.00447.2005

1001   74.   Döring B, Pfitzer G, Adam B, Liebregts T, Eckardt D, Holtmann G, et al. Ablation of
1002   connexin43 in smooth muscle cells of the mouse intestine: Functional insights into
1003   physiology and morphology. Cell Tissue Res. 2007;327: 333–342. doi:10.1007/s00441-
1004   006-0281-6

1005   75.   Harris AL. Connexin channel permeability to cytoplasmic molecules. Prog Biophys Mol
1006   Biol. 2007;94: 120–143. doi:10.1016/j.pbiomolbio.2007.03.011

1007   76.   Weber PA, Chang HC, Spaeth KE, Nitsche JM, Nicholson BJ. The permeability of gap
1008   junction channels to probes of different size is dependent on connexin composition and
1009   permeant-pore affinities. Biophys J. 2004;87: 958–973. doi:10.1529/biophysj.103.036350

1010   77.   Aliev RR, Richards W, Wikswo JP. A simple nonlinear model of electrical activity in the
1011   intestine. J Theor Biol. 2000;204: 21–28. doi:10.1006/jtbi.2000.1069

1012   78.   Barth BB, Henriquez CS, Grill WM, Shen X. Electrical stimulation of gut motility guided by
1013   anin silicomodel. J Neural Eng. 2017;14: 66010. doi:10.1088/1741-2552/aa86c8

1014   79.   Sneyd J, Charles AC, Sanderson MJ. A model for the propagation of intercellular calcium
1015   waves. Am J Physiol - Cell Physiol. 1994;266: 293–302.
1016   doi:10.1152/ajpcell.1994.266.1.c293

1017   80.   Allbritton NL, Meyer T, Stryer L. Range of messenger action of calcium ion and inositol
1018   1,4,5-trisphosphate. Science (80-). 1992;258: 1812–1815. doi:10.1126/science.1465619

1019   81.   Moshkforoush A, Balachandar L, Moncion C, Montejo KA, Riera J. Unraveling ChR2-
1020   driven stochastic Ca2+ dynamics in astrocytes: A call for new interventional paradigms.

44

1021   PLOS Comput Biol. 2021;17: e1008648. doi:10.1371/journal.pcbi.1008648

1022   82.   Ermentrout GB, Kopell N. Frequency Plateaus in a Chain of Weakly Coupled Oscillators,
1023   I. SIAM J Math Anal. 1984;15: 215–237. doi:10.1137/0515019

1024   83.   Furness JB, Jones C, Nurgali K, Clerc N. Intrinsic primary afferent neurons and nerve
1025   circuits within the intestine. Prog Neurobiol. 2004;72: 143–164.
1026   doi:10.1016/j.pneurobio.2003.12.004

1027   84.   Irisawa H, Brown HF, Giles W. Cardiac pacemaking in the sinoatrial node. Physiol Rev.
1028   1993;73: 197–227. doi:10.1152/physrev.1993.73.1.197

1029   85.   Ahmed MA, Jung R. Modeling of Slow Waves in the Stomach BT - Encyclopedia of
1030   Computational Neuroscience. Jaeger D, Jung R, editors. New York, NY: Springer New
1031   York; 2020. pp. 1–9. doi:10.1007/978-1-4614-7320-6_100704-1

1032   86.   Fall CP, Keizer JE. Mitochondrial modulation of intracellular Ca2+ signaling. J Theor Biol.
1033   2001;210: 151–165. doi:10.1006/jtbi.2000.2292

1034   87.   Höfer T. Model of intercellular calcium oscillations in hepatocytes: Synchronization of
1035   heterogeneous cells. Biophys J. 1999;77: 1244–1256. doi:10.1016/S0006-
1036   3495(99)76976-6

1037
1038

1039

1040 **Supporting information**

1041 **S1 Table. Summary of published models for a gastric slow-wave in the stomach.**

Model	Nature of modeling	Single ICC	Single SM cell	ICC chain (1-D)	ICC+SM cell network (2-D)	Enteric neuron network	Comparison with Experimental data			IP$_3$ Dynamics	Gap junction connectivity
							Animal model	Intact freq.	Intrinsic freq.		
Corrias & Buist, 2008	Biophysical	√	×	×	×	×	Guinea-pig antrum	N/A	√	N/A	N/A
Corrias & Buist, 2007	Biophysical	×	√	×	×	×	Canine antrum SMC	N/A	√	N/A	N/A
Peng Du, 2010	Biophysical	√	×	√	×	×	Simulated in mouse jejunum	N/A	N/A	Dynamic IP$_3$	Electrical
Buist, 2010	Biophysical	√	√	√	√	×	Guinea-pig stomach SMC	×	Antrum-(√) Corpus-(×)	Static IP$_3$	Electrical
Aliev, 2000	Coupled chain oscillator	√	√	√	√	×	Canine intestine	√	√	N/A	Electrical
Edwards, 2006	Electrical	√	√	√	√	×	Guinea-pig antrum SMC	N/A	√	N/A	Electrical
Barth, 2017	Electrical+ Biophysical	√	√	√	√	√	Rat colon	N/A	N/A	N/A	Electrical, synaptic and neuromuscular
Van Helden, 2003	Lumped biophysical	√	×	√	×	×	Guinea-pig pylorus SMC	N/A	N/A	Dynamic IP$_3$	Electrical & Chemical (Ca^{2+} & IP$_3$)
Our model	Biophysical	√	√	√	√	×	Cat & dog stomach	√	Antrum-(√) Corpus-(√)	Dynamic IP$_3$	Electrical & Chemical (Ca^{2+} & IP$_3$)

1042   **S2 Table. *Total Lag* under different values of $G_{ICC-ICC}$.** Mean ± standard deviation for the last

1043   7 cycles in each simulation.

$G_{ICC-ICC}$ value (nS)	Total Lag (sec)
0.35	53.77 ± 3.63
0.53	21.99 ± 0.02
0.7	20.85 ± 0.02
1.05	19.27 ± 0.03
1.4	18.22 ± 0.03
2.0	16.93 ± 0.03
3.0	15.51 ± 0.03
5.0	13.81 ± 0.03

1044

1045   **S3 Table. *SM Cell Period* under different values of $G_{ICC-ICC}$.** Mean ± standard deviation for the

1046   last 7 cycles in each simulation.

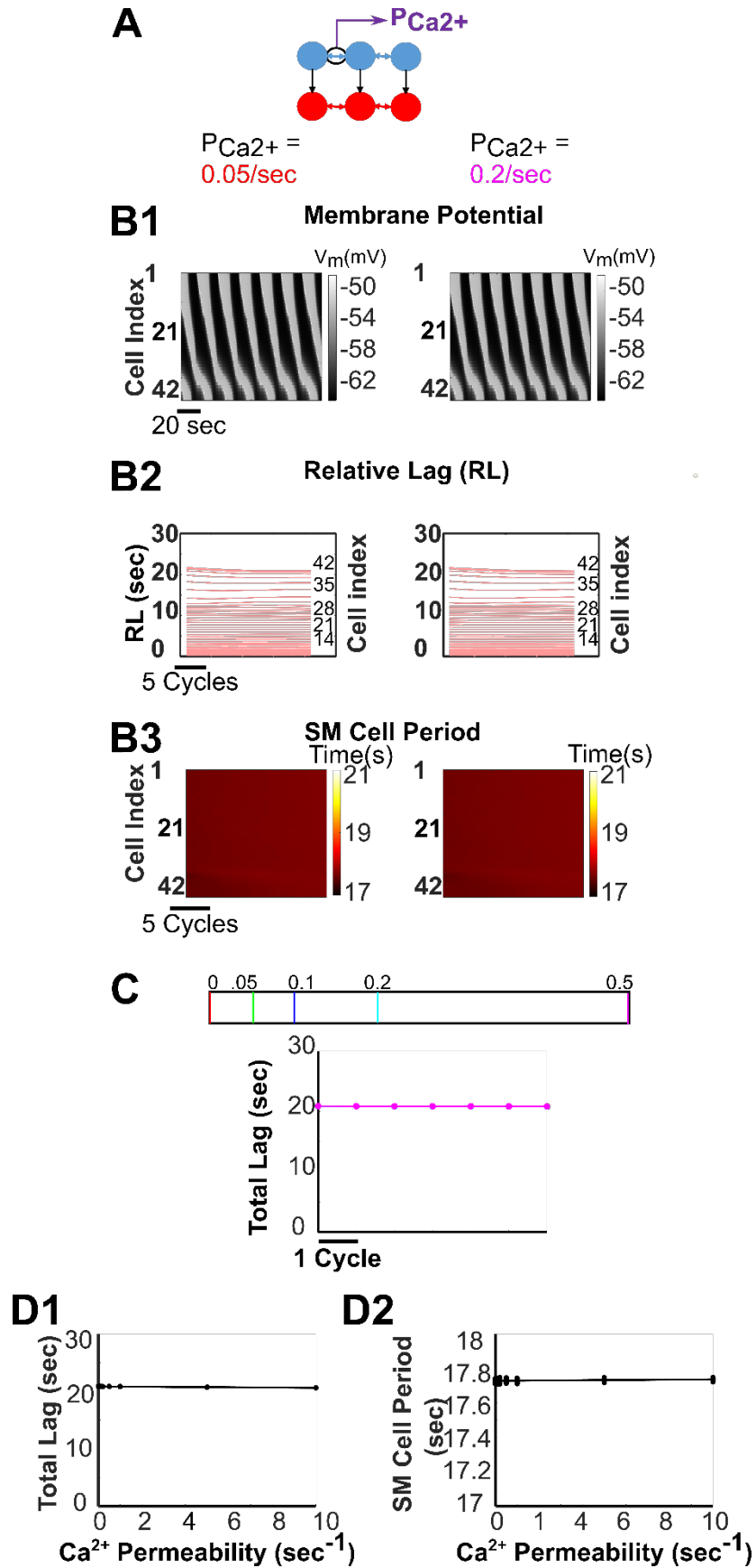| $G_{ICC-ICC}$ value (nS)	SM_1 Period (sec)	SM_{42} Period (sec)
0.35	17.75 ± 0.01	19.41 ± 0.44
0.53	17.75 ± 0.01	17.74 ± 0.03
0.7	17.74 ± 0.01	17.73 ± 0.01
1.05	17.70 ± 0.01	17.69 ± 0.01
1.4	17.67 ± 0.01	17.66 ± 0.01
2.0	17.64 ± 0.01	17.62 ± 0.01
3.0	17.59 ± 0.01	17.58 ± 0.01
5.0	17.52 ± 0.01	17.51 ± 0.01

1047

1048

47

1049 **S4 Table.** *Total Lag* **under different values of** P_{IP3}**.** Mean ± standard deviation for the last 7

1050 cycles in each simulation.

| P_{IP3} value (sec^{-1})	Total Lag (sec)
4.0	69.56 ± 2.45
6.0	53.99 ± 4.03
8.0	20.85 ± 0.02
12.0	16.85 ± 0.03
16.0	13.17 ± 0.03
20.0	10.92 ± 0.02
30.0	8.90 ± 0.01
40.0	7.93 ± 0.03

1051

1052 **S5 Table.** *SM Cell Period* **under different values of** P_{IP3}**.** Mean ± standard deviation for the last

1053 7 cycles in each simulation.

p_{IP3} value (sec^{-1})	SM$_1$ Period (sec)	SM$_{42}$ Period (sec)
4.0	17.31 ± 0.01	18.44 ± 0.34
6.0	17.53 ± 0.02	19.31 ± 0.59
8.0	17.74 ± 0.01	17.73 ± 0.01
12.0	17.94 ± 0.01	17.92 ± 0.01
16.0	18.31 ± 0.01	18.30 ± 0.01
20.0	18.58 ± 0.01	18.57 ± 0.01
30.0	18.69 ± 0.02	18.69 ± 0.01
40.0	18.71 ± 0.03	18.69 ± 0.02

A

$P_{Ca2+} =$
0.05/sec

$P_{Ca2+} =$
0.2/sec

B1 **Membrane Potential**

B2 **Relative Lag (RL)**

B3 **SM Cell Period**

C

0   .05   0.1   0.2   0.5

D1

D2

1054

49

1055   **S6 Fig. Increasing Ca²⁺ permeability across ICC-ICC gap junctions has no impact on network**

1056   **behavior. (A)** The network. **(B)** Spatiotemporal map of membrane potential **(B1)**, *Relative Lags* **(B2)**, and

1057   spatiotemporal map of *SM Cell Periods* **(B3)** for the network when P_{Ca2+} = 0.05 sec⁻¹ (left panel diagrams)

1058   and 0.2 sec⁻¹ (right panel diagrams). **(C)** The *Total Lags* for changes in P_{Ca2+} are shown for the last 7 cycles

1059   of 900-sec simulations. The corresponding values of these permeabilities in sec⁻¹ are shown in the legend.

1060   **(D)** For several networks, the mean *Total Lag* **(D1)** and the *SM Cell Period* **(D2)** of the last 7 cycles for each

1061   network with respect to its P_{Ca2+} are fit by an approximately constant line.

1062
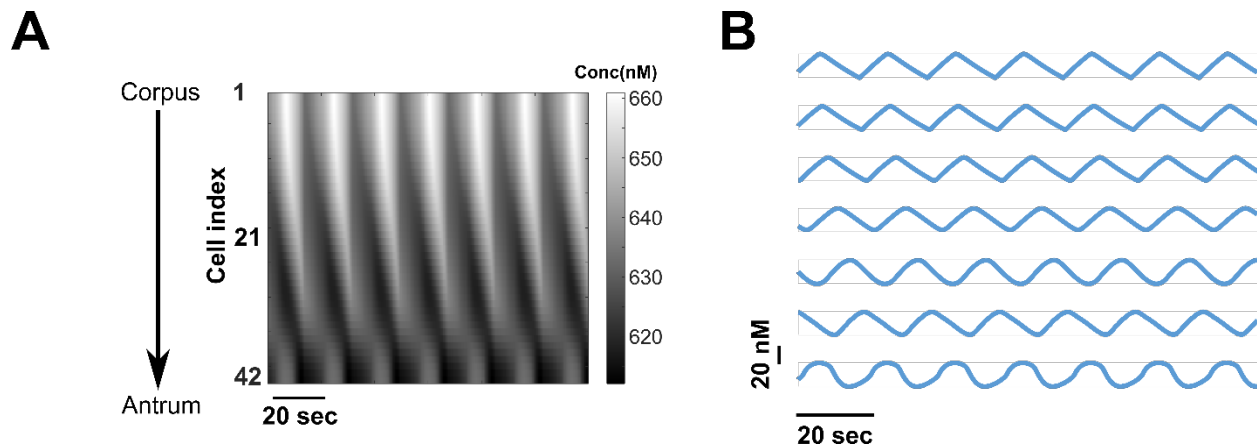
1063

1064   **S7 Fig. Spatiotemporal change in intracellular IP₃ concentration. (A)** Heatmap for all the cells in the

1065   network, and **(B)** for every 7ᵗʰ cell in the network in steady-state.

50
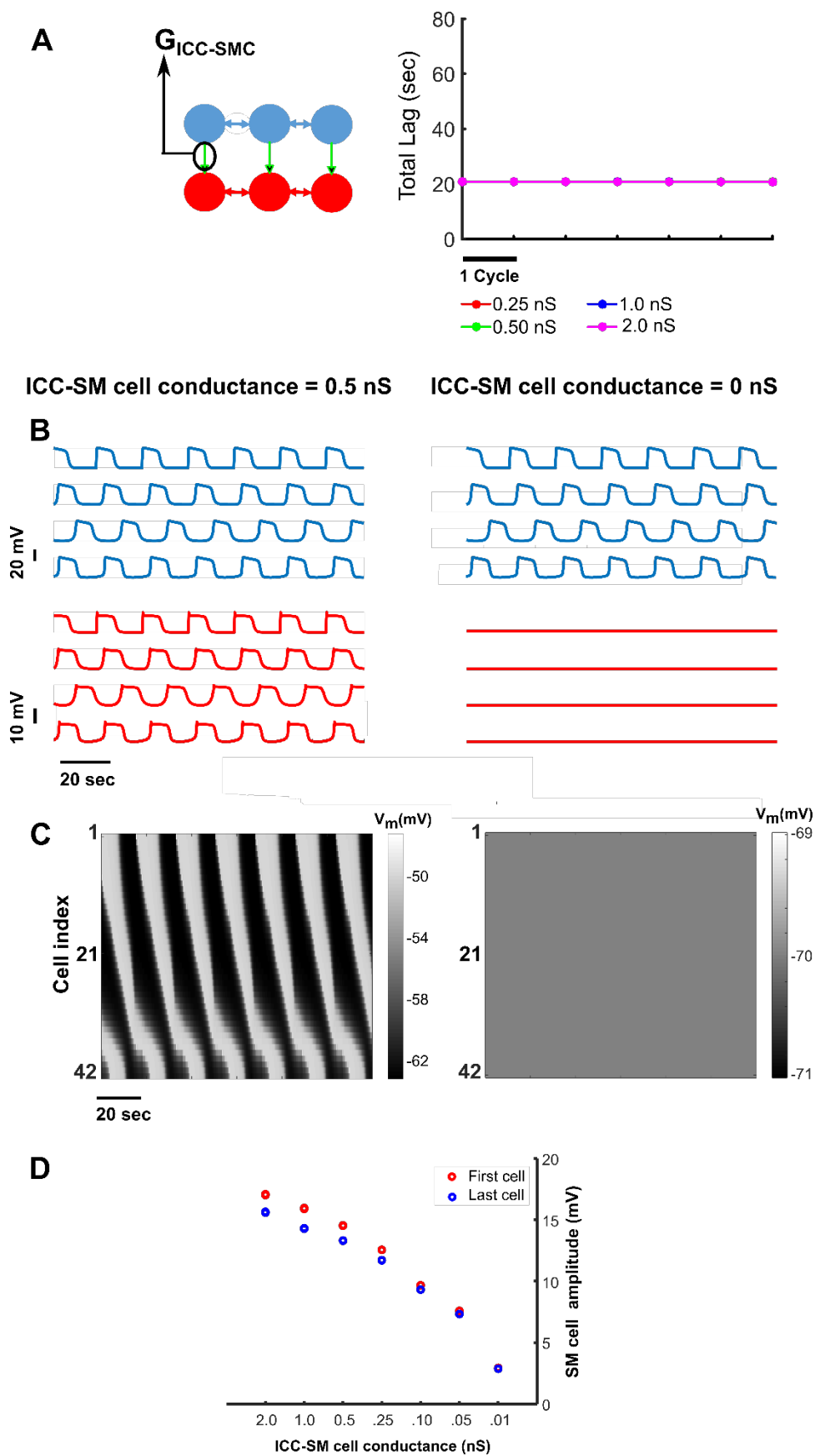
1067 **S8 Fig. The ICC-SM cell gap junction conductance impacts the SM cell membrane potential**

1068 **amplitude. (A)** ICC-SM cell electrical conductance does not have any effect on network entrainment

1069 evident from the approximately equal values of *Total Lag* measured for 4 different values of ICC-SM cell

1070 electrical conductances. **(B)** Membrane potential of 4 equidistant ICCs (top diagrams) and SM cells

1071 (bottom panel diagrams) in the 42-cell network when ICC-SM cell conductance is 0.5 ns (**left**) and 0 ns

1072 (**right**). **(C)** Spatiotemporal map of membrane potential of all 42 SM cells of the network, where ICC-SM

1073 cell conductance is 0.5 nS (**left**) and 0 nS (**right**). **(D)** Reduction of ICC to SM cell gap junction

1074 conductance reduces the amplitude of SM cell membrane potentials. For representation purposes, here

1075 the amplitudes (the peak-to-valley) of membrane potentials of the first and last SM cells of the network

1076 are shown.

1077